Chemical Engineering Journal 456 (2023) 141118

Contents lists available at ScienceDirect

Chemical Engineering Journal

journal homepage: www.elsevier.com/locate/cej

Coral-like porous microspheres comprising polydopamine-derived N-doped C-coated $MoSe_2$ nanosheets composited with graphitic carbon as anodes for high-rate sodium- and potassium-ion batteries

Jae Seob Lee [a,b,1], Jin-Sung Park [b,1], Kun Woo Baek [a,1], Rakesh Saroha [a], Su Hyun Yang [b], Yun Chan Kang [b,*], Jung Sang Cho [a,*]

[a] Department of Engineering Chemistry, Chungbuk National University, Chungbuk 361-763, Republic of Korea
[b] Department of Materials Science and Engineering, Korea University, Anam-Dong, Seongbuk-Gu, Seoul 136-713, Republic of Korea

ARTICLE INFO

Keywords:
Spray pyrolysis
Coral-like porous structure
Nitrogen-doped carbon
Molybdenum diselenide anode
Sodium-ion batteries
Potassium-ion batteries

ABSTRACT

Here, an innovative strategy for the synthesis of coral-like porous microspheres comprising polydopamine-derived N-doped C-coated $MoSe_2$ composited with graphitic carbon (Coral $MoSe_2$-GC@N—C) for use as advanced anode materials for sodium- and potassium-ion batteries (SIBs and PIBs) is introduced. The prepared composite is comprised of few-layered $MoSe_2$ particles with enlarged interlayer spacing, which are encapsulated within the graphitic carbon matrix, which acts as an efficient transport pathway for electrons. It is also characterized by the 3D interconnected pores derived from decomposition of polystyrene nanobeads, which ensure high contact area between the electrode and electrolyte and shortened sodium- and potassium-ion diffusion length. N-doped C with high electrical conductivity is coated uniformly on the surface, which plays the role of reinforcing the structural integrity as well as providing additional conductive pathway for facile electron transport. When applied as anodes for both SIBs and PIBs, the microspheres show good structural robustness and high rate capability. The anode exhibits high structural integrity, where stable cycle performance up to 200 cycles at 2.0 A/g for SIBs and 150 cycles at 1.0 A/g for PIBs was observed. In terms of rate performance, the anode exhibited high discharge capacities of 82 mA h g^{-1} (at 25 A/g, SIBs) and 152 mA h g^{-1} (at 10 A/g, PIBs), which clearly demonstrates the structural merits of the prepared microspheres.

1. Introduction

In the recent years, sodium- and potassium-ion batteries (SIBs and PIBs) have gained tremendous research attention due to their potential in replacing lithium-ion batteries (LIBs), which utilizes Li element with uneven geological distribution on earth and high price due to the scarcity [1–5]. Unfortunately, the practical use of SIBs and PIBs is hindered due to the critical problems including capacity decay arising from repetitive insertion and extraction of Na- and K-ions and sluggish electrochemical kinetics due to the larger ionic radius of Na-ion (1.02 Å) and K-ion (1.38 Å) in comparison to that of Li-ion (0.76 Å) [1,2,5–7]. Various approaches have been adopted to enhance the electrochemical performance of anode materials applied for SIBs and PIBs [5–9]. For achieving high capacity, various transition metal chalcogenides have been applied as anodes due to their high theoretical capacity [10–16]. Among them, $MoSe_2$ material with large interlayer spacing of 0.63 nm has been thoroughly investigated due to their efficient ingress and egress of Na- or K-ions between the layers [17–19]. Unfortunately, $MoSe_2$ materials suffer from structural degradation due to the volume changes that inevitably occur during cycling [19,20]. In addition, due to the high surface energy, $MoSe_2$ nanosheets are prone to agglomerate during preparation procedure [19,21].

Design of nanostructured electrode materials has proven effective in enhancing the electrochemical properties of anode materials for both SIBs and PIBs [17,22–24]. One of the most successful approaches is to introduce pores inside electrode materials, which can accommodate the large strain induced during repetitive cycles, endow large contact area between the active material and the electrolyte, and shorten the alkali-ion diffusion length [17,22,25]. Various methods have been applied for the synthesis of porous electrode materials; Zhang et al. prepared

* Corresponding authors.
E-mail addresses: yckang@korea.ac.kr (Y.C. Kang), jscho@cbnu.ac.kr (J.S. Cho).
[1] These authors contributed equally to this work.

https://doi.org/10.1016/j.cej.2022.141118
Received 16 October 2022; Received in revised form 6 December 2022; Accepted 20 December 2022
Available online 22 December 2022

multicore-shell FeS_2@C nanocapsules for use as anode for PIBs by coating Fe_2O_3 nanocapsule with carbon, etching with HF solution, and subsequent sulfidation process. The numerous pores in the anode enabled effective alleviation of volume changes, where capacity retention of 84.2 % after 500 cycles at 0.5 A g^{-1} was observed [26]. Wang et al. successfully prepared ultrafine SnO_2 nanoparticles anchored on 3D porous carbon network as anode for PIBs; high rate performance (145 mA h g^{-1} at 2.0 A g^{-1}) was observed since the porous structure enabled facile penetration of electrolyte, enlarging the contact area with the anode [27]. Since many strategies for the synthesis of porous materials are based on the multiple coating steps and the use of etchants, simpler and more safe methods should be developed.

Compositing active materials with carbonaceous matrix is also spotlighted as an effective approach for improving the electrochemical performance of anode materials [28–30]. Conductive carbon such as graphitic carbon (GC) can extend battery life, compensate for the low electrical conductivity of transition metal chalcogenides, and provide conductive pathways for efficient ion and electron transport [30,31]. Besides, carbon coating has been a promising method to enhance the electrochemical properties of $MoSe_2$-based materials, which can inhibit the stacking and crystal growth of $MoSe_2$, overcome the low electron transport kinetics, and alleviate the volume variation during the discharge/charge process [21,32]. In particular, N-doped C coating has been an effective strategy to enhance the electrochemical performance of both SIBs and PIBs [21,33,34]. Nitrogen doping into the carbon material can tune the electron-donor properties, and consequently improve the electrical conductivity of the carbon material and increase the bonding force between the carbon materials and $MoSe_2$ [33–35]. In addition, it not only improves the utilization of the active material by preventing poly-selenide dissolution problem after the first cycle, but also triggers the formation of a stable solid electrolyte interphase (SEI) layer leading to stable cycle performance [35].

To effectively restrict the agglomeration of $MoSe_2$ material, we introduced a 3-dimensional (3D) interconnected porous structure that comprises $MoSe_2$ nanocrystals well-embedded inside the GC matrix using spray pyrolysis process. In this study, a facile strategy for the preparation of coral-like porous microspheres comprising polydopamine (PDA)-derived N-doped C-coated $MoSe_2$ composited with GC (Coral $MoSe_2$-GC@N—C) is introduced. Aqueous solution containing ammonium molybdate, polyvinylpyrrolidone (PVP), and polystyrene (PS) nanobeads, each of which plays an important role in the synthetic procedure, was atomized using ultrasonic power. During pyrolysis, 3D-interconnected porous structure is developed in the microspheres due to the decomposition of PS nanobeads. The growth of $MoSe_2$ crystals and their stacking are inhibited since molybdenum component is encapsulated within PVP matrix during the synthetic procedure. During selenization process, GC is formed from the graphitization of PVP due to the catalytic effect of metallic Mo nuclei, which acts as primary transport pathway by which electrons are directly transferred from the active material. Subsequently, N-doped C derived from PDA was coated on the microspheres to not only reinforce the structural integrity but also act as a secondary pathway for electron transport. The formation mechanism of Coral $MoSe_2$-GC@N—C microspheres is systematically investigated at each synthesis step, by analyzing the characteristics of the microspheres in depth. These structural merits altogether led to enhanced electrochemical properties as anodes for both SIBs and PIBs, especially in terms of rate performances.

2. Experimental

2.1. Sample preparation

Coral-like porous microspheres comprising PDA-derived N-doped C-coated $MoSe_2$ composited with GC are prepared by spray pyrolysis process, subsequent heat treatment, and liquid-based coating process. Briefly, 12 g of $(NH_4)_6Mo_7O_{24}{\cdot}4H_2O$ (DAEJUNG, >98 %) and 4 g of PVP (DAEJUNG, M_w = 40,000) were dissolved in 200 mL of distilled water by vigorous stirring for 2 h. Subsequently, 200 mL of 0.1 g mL^{-1} PS nanobead suspension (ϕ = 100 nm) was added and stirred for a couple of hours to obtain the colloidal spray solution. PS nanobeads were prepared using the method described in our previous report [36]. The prepared suspension was ultrasonically nebulized into droplets, which were then carried to a quartz reactor fixed at 700 ℃ using N_2 carrier gas (10 L min^{-1}). The as-prepared powder obtained through the spray pyrolysis was subjected to heat treatment in a slightly reducing atmosphere [Ar/H_2 (vol = 95:5%) mixture gas] at 350 ℃ for 3 h for the selenization process. The weight ratio of Se powder, which is used as the Se source, and as-prepared powder was 3:1. 0.1 g of the as-prepared porous $MoSe_2$-GC microspheres was dispersed in 100 mL of tris buffer solution (0.01 M, pH: 8.7), and then 50 mg dopamine hydrochloride (Alfa Aesar, 99 %) was added and stirred at ambient condition for 12 h. PDA-coated porous $MoSe_2$-GC microspheres were washed with distilled water several times using centrifugation, and then dried in an oven at 100 ℃. Finally, Coral-like porous microspheres comprising PDA-derived N-doped C-coated $MoSe_2$ composited with GC were obtained by carbonization process at 400 ℃ for 3 h in an N_2 atmosphere. For comparison, bare $MoSe_2$ powder was also prepared through an identical method using spray pyrolysis and selenization process. The spray solution was prepared from addition of 12 g $(NH_4)_6Mo_7O_{24}{\cdot}4H_2O$ to 400 mL distilled water and subsequent stirring for 1 h. The temperature of the quartz reactor was fixed at 400 ℃, and flow rate of the carrier gas (air) was 10 L min^{-1}. The as-prepared MoO_x microspheres without pores and carbon obtained by spray pyrolysis were selenized at 500 ℃ for 10 h under Ar/H_2 (vol = 95:5%) atmosphere to obtain bare $MoSe_2$ powders. Additional information on material characterization and electrochemical characterization is provided in the supporting information.

3. Results and discussion

Coral-like porous microspheres comprising PDA-derived N-doped C-coated $MoSe_2$ composited with GC were prepared from spray pyrolysis, and subsequent selenization and C-coating processes. The detailed synthesis mechanism for unique-structured porous microspheres is systematically described in Scheme 1. Aqueous droplets composed of ammonium molybdate, PVP, and PS nanobeads (ϕ = 100 nm) as Mo precursor, carbon source, and porogen, respectively, were generated

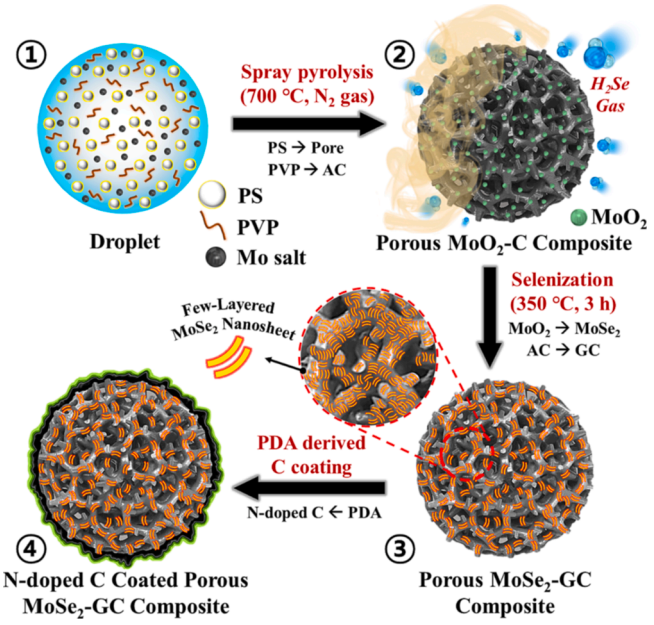

Scheme 1. Schematic representation of formation mechanism(①-④) of Coral $MoSe_2$-GC@N—C composite microspheres.

using ultrasonic nebulizer. (Scheme 1-①). The droplets goes through a vertical quartz reactor tube (Scheme S1) which was maintained at 700 °C; in this process, Mo precursor is thermally decomposed to MoO_2 and PVP is transformed into amorphous carbon (AC). PS nanobeads are eliminated during spray pyrolysis leaving pores behind, resulting in the formation of interconnected mesoporous structure throughout the whole microsphere. This resulted in the formation of porous composite microspheres with single phase MoO_2 embedded in the AC matrix (Scheme 1-②). Furthermore, the as-sprayed porous MoO_2-C composite microspheres were selenized at 350 ℃ for 3 h in the Ar/H_2 (vol = 95:5%) atmosphere. During selenization, MoO_2 reacted with H_2Se gas, which is generated from the reaction of Ar/H_2 with Se, and metallic Mo nuclei and SeO_2 were formed. The components sublimated at temperatures above 315 °C, and $MoSe_2$ phase was subsequently formed [37]. In addition, the AC decomposed from PVP was further converted to GC by the assistance of Mo as a catalyst for graphitization [38–40]. Moreover, numerous pores formed by the decomposition of PS nanobeads facilitated the penetration of H_2Se gas into the interior of the structure, enabling the homogeneous formation of $MoSe_2$ crystals throughout the microspheres. The selenization process led to the formation of coral-like porous microspheres comprising $MoSe_2$ composited with GC (denoted as Coral $MoSe_2$-GC; Scheme 1-③). In the final step, PDA-derived N-doped C layer, which acts as a secondary conductive pathway, was coated onto Coral $MoSe_2$-GC composite microspheres through a facile solution-based coating process. Coral $MoSe_2$-GC microspheres treated with PDA were carbonized at 400 ℃ in an N_2 atmosphere, which formed uniform N-doped C coating on the surface (Scheme 1-④). The overall synthesis process led to the formation of highly conductive coral-like porous microspheres comprising PDA-derived N-doped C-coated $MoSe_2$ composited with GC (denoted as Coral $MoSe_2$-GC@N—C).

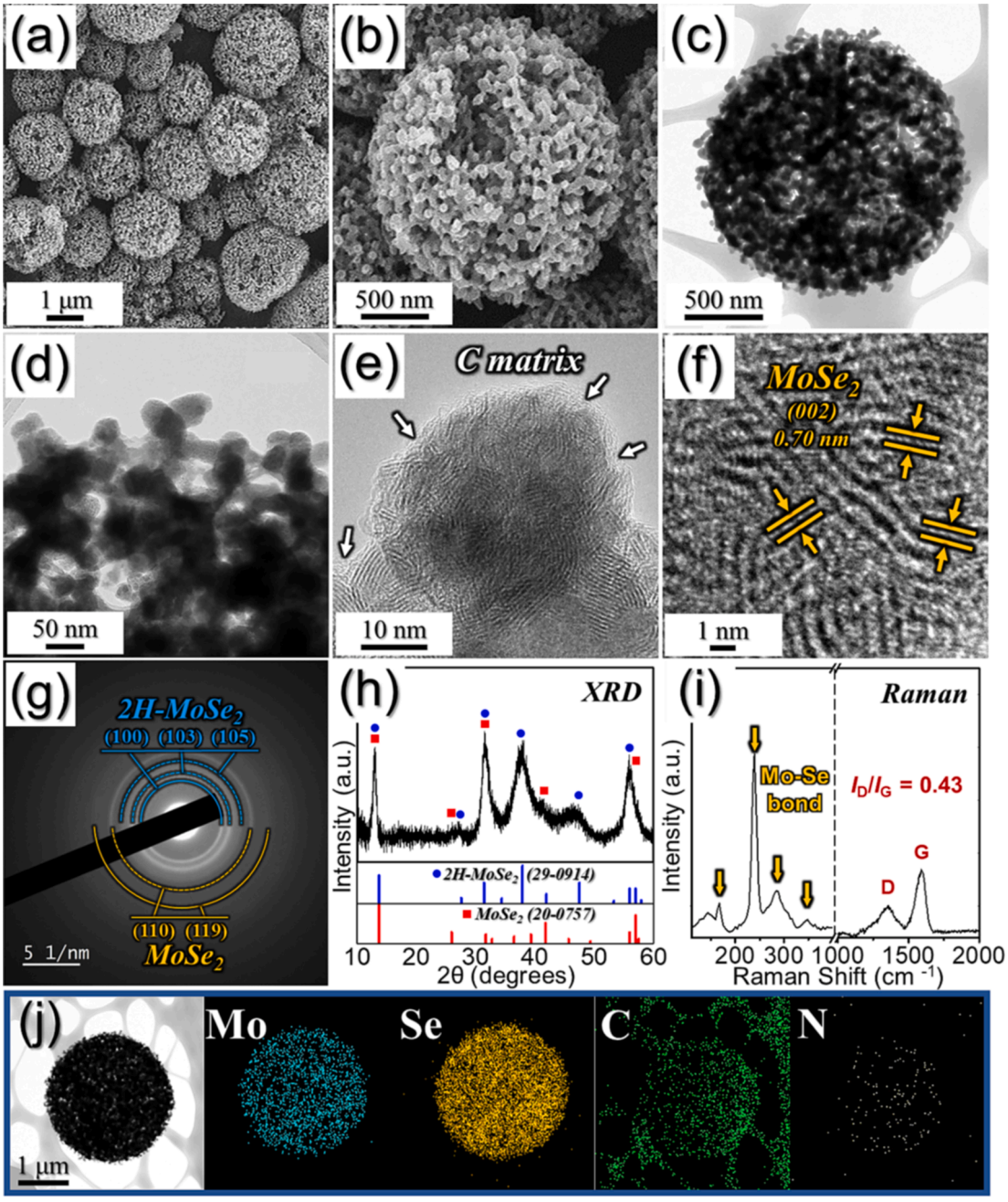

Fig. 1. Morphologies, SAED, XRD pattern, Raman spectrum, and elemental mapping images of Coral $MoSe_2$-GC composite microspheres obtained after selenization at 350 ℃: (a,b) FE-SEM images, (c-e) TEM images, (f) HR-TEM image, (g) SAED pattern, (h) XRD pattern, (i) Raman spectrum, and (j) elemental mapping images.

After each step of the synthesis, comprehensive morphological and crystallographic analyses of the prepared microspheres were performed to elucidate the formation mechanism. Microstructure and XRD pattern of as-prepared porous MoO_2-C composite microspheres obtained from spray pyrolysis are shown in Fig. S1. The FE-SEM image (Fig. S1a) reveals the formation of well-dispersed and non-agglomerated microspheres with an average diameter of 1.5 μm. Moreover, the presence of interconnected open pores at the outer surface of the microspheres could be identified. In the fractured FE-SEM image shown in Fig. S1b, numerous interconnected pores could be witnessed, suggesting that interconnected pores also exist at the interior of the microspheres. The formation of these pores is due to the decomposition of PS nanobeads into gaseous products during spray pyrolysis at 700 ℃. The XRD pattern (Fig. S1c) of the powder shows well-resolved sharp diffraction peaks corresponding to MoO_2. TG analysis (Fig. S1d) of porous MoO_2-C composite was performed in an air atmosphere, which revealed some weight fluctuation as a function of temperature. The initial weight loss that occurs up to 200 ℃ is due to the removal of water molecule adsorbed on the surface as well as water in the crystal lattice. Weight increase at 360 ℃ and subsequent weight loss at temperature range of 360–440 ℃ correspond to the oxidation reaction of MoO_2 to form MoO_3 and decomposition of carbon into gaseous products, respectively, where total of 5 wt% weight loss was observed. Since a theoretical weight gain of 10 wt% occurs when MoO_2 is transformed into MoO_3 phase, the weight loss due to the combustion of carbon corresponds to 15 wt%, which is in line with the elemental analysis (EA) results of porous MoO_2-C microspheres shown in Table S1.

The coral-like porous microspheres comprising $MoSe_2$ composited with GC (Coral $MoSe_2$-GC) were obtained by selenization of as-sprayed porous MoO_2-C composite. Selenium powder was adopted as Se source since it can combine with H_2 to form H_2Se gas during the heat-treatment process. The morphological and crystallographic characteristics of Coral $MoSe_2$-GC microspheres obtained from the selenization process are shown in Fig. 1. The low magnification FE-SEM image (Fig. 1a) clearly indicates that the obtained Coral $MoSe_2$-GC microspheres (average diameter ≈ 1.5 μm) were non-agglomerated with well-distributed interconnected mesopores present at the external and internal parts of the microspheres (Fig. 1b). The TEM image (Fig. 1c) further confirms that numerous pores were formed inside the microspheres. The TEM image in Fig. 1d reveals the crystalline $MoSe_2$ and numerous mesopores with dark and bright contrast, respectively. The magnified TEM image (Fig. 1e) shows that polycrystalline few-layered $MoSe_2$ nanosheets with an average width of 5 nm are embedded within the carbon matrix. Polycrystalline few-layered nanosheets were formed since the crystal growth and stacking of the nanosheets were effectively suppressed by the surrounding carbon material. Moreover, it should be noted that the interconnected pores generated by the decomposition of PS nanobeads allow efficient penetration of H_2Se gas into the structure, forming uniform polycrystalline few-layered nanosheets throughout the microspheres. Polycrystalline few-layered $MoSe_2$ nanosheets in the carbon matrix is expected to increase the contact with the electrolyte, thereby improving the ionic/electronic conductivity. The high-resolution TEM (HR-TEM) image (Fig. 1f) shows well-resolved interlayer spacing of 0.70 nm corresponding to the (002) lattice plane of $MoSe_2$, which is slightly wider than that of natural $MoSe_2$ (0.63 nm). NH^{4+} ions, which are derived from ammonium molybdate salt and incorporated between the lattices of molybdenum compound, were removed during the selenization process, widening the interlayer spacing [41,42]. It is expected that the expanded lattice spacing can accelerate the intercalation/deintercalation kinetics of Na- and K-ions, therefore enhancing the reversible capacity and rate capability of the electrode. The selected area electron diffraction (SAED) pattern (Fig. 1g) displays well-resolved diffraction rings that correspond to the bi-phasic crystal lattices of 2H-$MoSe_2$ and $MoSe_2$. The XRD pattern (Fig. 1h) exhibits sharp peaks relevant to the mixed phases of 2H-$MoSe_2$ and $MoSe_2$, which is consistent with the SAED results. Additionally, the average crystallite size of $MoSe_2$ in Coral $MoSe_2$-GC microspheres calculated from the Scherrer equation using the highly intense (100) diffraction peak in the XRD pattern was 5.3 nm; the result matches well with the TEM results. The Raman spectrum (Fig. 1i) of Coral $MoSe_2$-GC microspheres shows the peaks at 167.1, 239.1, 284.5, and 348.0 cm^{-1} corresponding to in-plane vibration of E_{1g}, out-of-plane A_{1g}, in-plane E^1_{2g}, and B^1_{2g} mode of $MoSe_2$, respectively [43,44]. The peaks at 1358 and 1589 cm^{-1} can be assigned to the D- and G-band of the carbon material, respectively [43]. In addition, the relative intensity ratio of the D- and G-band (I_D/I_G), which can be used as an indicator to determine the crystallinity of carbon materials, of 0.43 suggests the highly crystalline nature of carbon. Compared to the I_D/I_G ratio of as-sprayed microspheres (Fig. S2), Coral $MoSe_2$-GC microspheres exhibited much lower I_D/I_G value. This is because AC was converted to GC due to the catalytic effect of metallic Mo nuclei formed during the selenization process in a reducing atmosphere. Additionally, the estimated C content in Coral $MoSe_2$-GC microspheres through TG analysis (Fig. S3) was 5 wt%, which is consistent with the EA results (Table S1). The elemental mapping results (Fig. 1j) reveal the homogeneous distribution of Mo, Se, C, and N in Coral $MoSe_2$-GC microspheres.

In order to achieve excellent Na- and K-ion storage performance of the cell with high-rate capability and reasonable cycling stability, PDA-derived N-doped C was coated on Coral $MoSe_2$-GC microspheres through a facile solution-based method and subsequent carbonization heat-treatment. The morphologies of coral-like porous microspheres comprising PDA-derived N-doped C-coated $MoSe_2$ composited with GC (Coral $MoSe_2$-GC@N—C) are provided in Fig. 2. The low-magnification FE-SEM image (Fig. 2a) shows that Coral $MoSe_2$-GC@N—C microspheres shares similarity with Coral $MoSe_2$-GC microspheres in terms of morphology. The high-magnification FE-SEM image (Fig. 2b) indicates that the coating and subsequent heat treatment process had a negligible effect on the overall morphologies of the composite microspheres. The TEM images (Fig. 2c and d) show coral-like porous microspheres comprising numerous interconnected pores throughout the structure. The high-magnification TEM image (Fig. 2e) reveals that carbon layer with a uniform coating thickness of 8.2 nm, which encompass the polycrystalline few-layered $MoSe_2$ nanosheets composited with GC, is formed after the coating process. This can be confirmed from the distribution of coated carbon in external and internal parts of the microspheres obtained using electron energy-loss spectroscopy (EELS) analysis (Fig. S4). As shown in the Fig. S4a, Mo, Se, and C elements were uniformly distributed in a single microsphere. Notably, near the surface of each primary particle comprising the microsphere, green dots corresponding to C element could be observed in the regions where blue and orange dots do not exist, suggesting the coverage of $MoSe_2$ particles by carbon. This is further confirmed from the magnified images showing the distribution of Mo and C elements near the pore and for dense particle (Fig. S4b and c), where carbon surrounding the $MoSe_2$ particles could be clearly observed. Additionally, the HR-TEM image (Fig. 2f) suggests that the coating process did not affect the crystal structure of the composite microspheres, which can be ascertained by the lattice fringe separated by 0.70 nm, corresponding to the (002) plane of $MoSe_2$. The SAED pattern (Fig. 2g) also shows clear diffraction rings corresponding to 2H-$MoSe_2$ and $MoSe_2$ phases, which is in line with that of coral $MoSe_2$-GC microspheres (Fig. 1h), confirming that $MoSe_2$ crystal phase was maintained even after additional heat treatment. The bi-phasic crystal lattices of 2H-$MoSe_2$ and $MoSe_2$ are uniformly distributed within the microspheres since the spray pyrolysis process was used for the synthesis. Powder prepared from spray processes include homogeneous composition since the desired metal salts and carbon sources are dissolved in the precursor solution at atomic scale. The HR-TEM images of Coral $MoSe_2$-GC@N—C composite microspheres were further analyzed (Fig. S5). Several interlayer spacing corresponding to 2H-$MoSe_2$ and $MoSe_2$ phases could be observed, confirming the homogenous distribution of both phases inside the microsphere. The

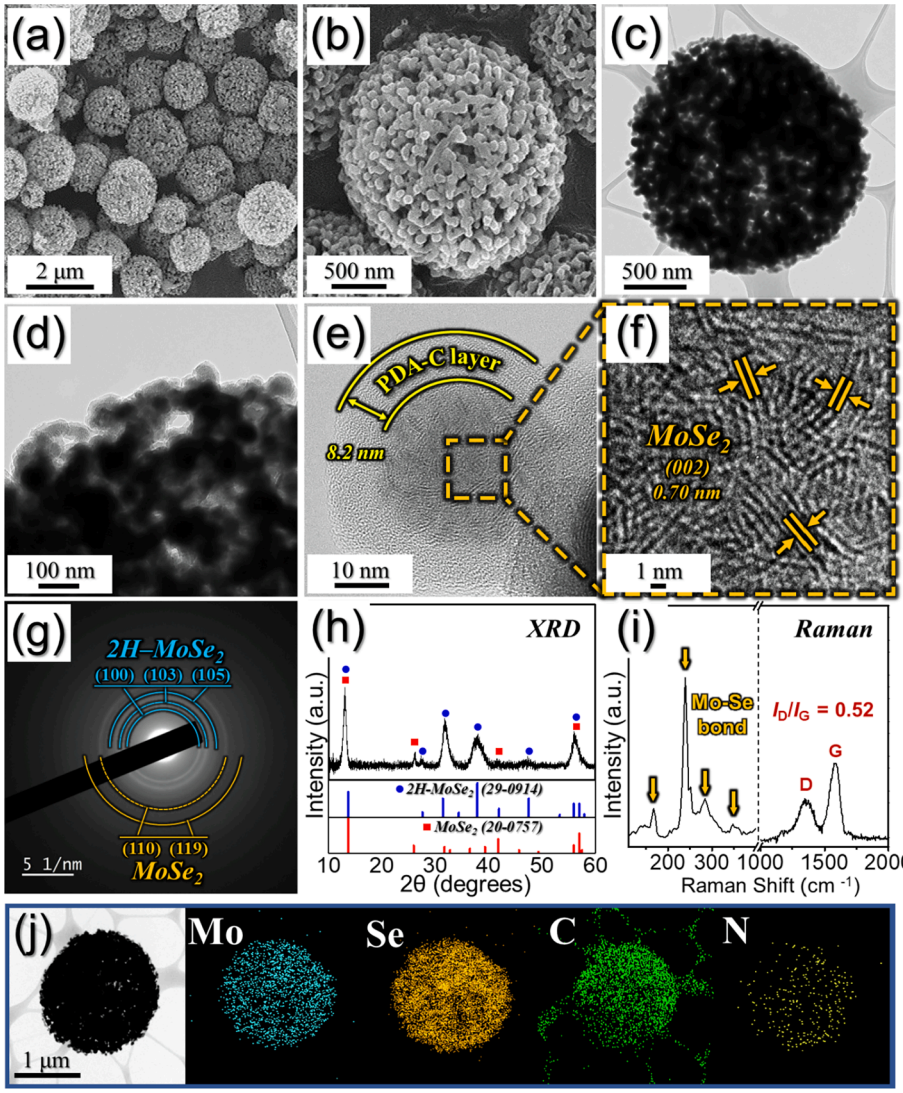

Fig. 2. Morphologies, SAED, XRD pattern, Raman spectrum and elemental mapping images of the Coral $MoSe_2$-GC@N—C composite microspheres: (a,b) FE-SEM images, (c-e) TEM images, (f) HR-TEM image, (g) SAED pattern, (h) XRD pattern, (i) Raman spectrum, and (j) elemental mapping images.

existence of both 2H-$MoSe_2$ and $MoSe_2$ phases uniformly distributed at nanoscale forms heterointerface. Therefore, it is expected that they can accelerate the electrochemical kinetics to a certain degree [45,46]. The XRD pattern (Fig. 2h) is in good agreement with the above results, indicating a clear coexistence of diffraction peaks corresponding to the nanocrystalline 2H-$MoSe_2$ and $MoSe_2$ crystal structures. The specific contents of 2H-$MoSe_2$ and $MoSe_2$ phases were quantified using Rietveld refinement, as shown in Fig. S6. Rietveld refinement was carried out using crystallographic information of 2H-$MoSe_2$ with a hexagonal structure (*P*63/*mmc* space group) and $MoSe_2$ with hexagonal structure (*R*3*m* space group). The phase fractions of 2H-$MoSe_2$ and $MoSe_2$ in Coral $MoSe_2$-GC@N—C composite microspheres were calculated as 36.2 mol % and 63.8 mol%, respectively. Notably, both the interlayer spacing of $MoSe_2$ in Coral $MoSe_2$-GC and Coral $MoSe_2$-GC@N—C microspheres showed blue shift as revealed by the XRD pattern in Fig. S7. The interlayer spacing calculated from the Bragg's law for Coral $MoSe_2$-GC (0.68 nm) and Coral $MoSe_2$-GC@N—C (0.68 nm) microspheres ascertained the enlarged interlayer spacing. There was some discrepancy between the interlayer spacing obtained from HR-TEM images (Fig. 1f and 2f) and XRD patterns (Fig. S7), which may have occurred due to different analysis methods, but both data revealed the enlarged interlayer spacing of $MoSe_2$ in Coral $MoSe_2$-GC and Coral $MoSe_2$-GC@N—C microspheres. The average crystallite size of $MoSe_2$ in Coral $MoSe_2$-GC@N—C microspheres was 6.5 nm, which was calculated using the Scherrer formula from (1 0 0) peak with high intensity in the XRD pattern. Even after further heat treatment, the average size of $MoSe_2$ nanocrystals was similar, suggesting effective inhibition of crystal growth by the carbon matrix and the PDA-derived C layer surrounding the $MoSe_2$ crystals. These results confirmed that $MoSe_2$ phase was maintained even after PDA treatment, and the thin PDA-derived C layer was uniformly coated on the polycrystalline few-layered $MoSe_2$ nanosheets composited with GC. In particular, the PDA-derived conductive C layer, along with GC, served as pathway for fast electron transport. Moreover, the carbon coating strategy not only increases the mechanical integrity of the composite microspheres, but also improves electrochemical properties due to the accelerated redox process. The Raman spectrum of Coral $MoSe_2$-GC@N—C microspheres (Fig. 2i) reveals characteristic peaks at 167.1, 239.2, 284.1, and 348.0 cm^{-1} of $MoSe_2$, identical to the Raman results of Coral $MoSe_2$-GC microspheres (Fig. 1i) [43,44]. In addition, Raman spectra of Coral $MoSe_2$-GC and Coral $MoSe_2$-GC@N—C microspheres in the Fig. S8 (in the range between 200 and 320 cm^{-1}) revealed peaks corresponding to A_{1g}/E^1_{2g} bands that occur at 239.1/284.5 cm^{-1} and 239.2/284.1 cm^{-1}, respectively. The peaks corresponding to the A_{1g} and E^1_{2g} bands were blue-shifted and red-shifted, respectively, in comparison to those of bulk $MoSe_2$ reported in the literatures [47–49],

which reveals the few-layered characteristics of $MoSe_2$ in Coral $MoSe_2$-GC and Coral $MoSe_2$-GC@N—C microspheres. Furthermore, peaks corresponding to the D- and G-band of the carbon material were observed at 1358 and 1582 cm^{-1}, and the I_D/I_G value was 0.52 [43]. This value also suggests the highly crystalline nature of carbon, however the I_D/I_G value higher than that of non-coated Coral $MoSe_2$-GC microspheres (0.43) indicated that the introduction of the PDA-derived C layer increased the disordered carbon in the nanostructure. The result shows that the abundant N dopant in the PDA-derived C layer introduced defects, resulting in the increase in the intensity of D-band and decrease in crystallinity. This observation is consistent with the EA results before and after the PDA coating process (Table S1). The N contents of Coral $MoSe_2$-GC@N—C and Coral $MoSe_2$-GC were 2.7 and 0.9 w%, respectively. PDA-derived N-doped C is expected to provide improved electrical conductivity and electrochemical reactivity of Coral $MoSe_2$-GC@N—C. Additionally, defects formed in the N-doped C layer could provide additional Na-ion insertion sites that enhance Na-ion storage ability. The elemental mapping results in Fig. 2j show the uniform dispersion of Mo, Se, C and N elements in Coral $MoSe_2$-GC@N—C microspheres. Overall, the above results indicate that PDA-derived N-doped C was successfully coated on polycrystalline few-layered $MoSe_2$ nanosheets composited with GC to support a kinetically favored redox process and further improve the overall electrochemical performance.

The chemical nature of Coral $MoSe_2$-GC@N—C microspheres was characterized by X-ray photoelectron spectroscopy (XPS). The XPS survey spectrum (Fig. 3a) consists of photoelectric signals corresponding to Mo 3d, Se 3d, C 1s, and N 1s. Mo 3d spectrum (Fig. 3b) shows two strong peaks at binding energies of 232.3 and 228.6 eV, which correspond to the Mo $3d_{3/2}$ and Mo $3d_{5/2}$ states of $MoSe_2$ [50,51]. The peaks corresponding to Mo–O bonding at 235.6 and 231.1 eV are attributed to partial surface oxidation of the samples upon exposure to air [19,50]. In the Se 3d spectrum (Fig. 3c), characteristic peaks at 55.2 eV (Se $3d_{3/2}$) and 54.1 eV (Se $3d_{5/2}$) of $MoSe_2$ are also observed [19,51]. Metalloid Se peaks are observed at 229.9 eV (Se 3s; Fig. 3b), 56.5 and 55.8 eV (Se 3d; Fig. 3c) due to the incorporation of metalloid Se into the structure during selenization [19,51]. However, the amount of intercalated Se is assumed to be low because the peak corresponding to Se was not detected in the XRD pattern (Fig. 1h) after selenization. Additionally, the Se-O peak at 58.5 eV is attributed to the SeO_2 formed by exposure of Coral $MoSe_2$-GC@N—C microspheres to the ambient atmosphere [19]. The C 1s spectrum (Fig. 3d) reveals three peaks corresponding to O-C═O, C—N/C—C, and C═C bonds at 288.9, 286.0, and 284.8 eV, respectively [19,52]. The high intensity of the C═C peak suggests the formation of GC during selenization process. Moreover, the C—N/C—C peak indicates the presence of N-doped C, and the types of bonding present in N-doped C bonds could be identified in the N 1s spectrum (Fig. 3e). The N 1s spectrum exhibits three peaks at binding energies of 402.5, 400.4, and 398.5 eV, corresponding to graphitic-N, pyrrolic-N, and pyridinic-N, respectively [53,54]. Graphitic-N was bonded to two C atoms at the edge of sp^2 carbon plane whereas pyridinic-N was bonded to three C atoms within the graphene plane, respectively [55]. The pyrrolic-N corresponds to the N atoms inside a five-membered heterocyclic ring [55]. In addition, Mo-N bond and Mo 3p signals were observed at 396.5 and 394.5 eV, respectively [53,54]. Mo-N bonds are most probably formed between $MoSe_2$ and N-doped C phase during the heating process [54]. To confirm the C content of Coral $MoSe_2$-GC@N—C microspheres, TG analysis was performed under an air atmosphere. The rapid weight loss of 53 wt% observed at 366–440 ℃ is due to the transformation of $MoSe_2$ into MoO_3 and combustion of organic elements, such as C and N (Fig. 3f). The weight loss that occurs from oxidation of $MoSe_2$ into MoO_3 and combustion of C and N was estimated to be *ca.* 34 and 19 wt%, respectively, which was consistent with the C content (15.9 wt%) and the N content (2.7 wt%) from the EA analysis results (Table S1). The N_2 adsorption–desorption isotherms of Coral $MoSe_2$-GC@N—C microspheres (Fig. S9a) suggest a high degree of gas adsorption, which can be attributed to the presence of interconnected macropores and micropores inside the microspheres and at external surfaces, which led to a high BET surface area of 55 $m^2\ g^{-1}$. The y-values peaked at < 2 and 57 nm of the Barrett-Joyner-Halenda (BJH) pore size curve (Fig. S9b), proving the presence of micro and macropores. Micropores originated from the N-species present in the PDA-derived C-coating layer which induced surface defects. In addition, macropores are attributed to the thermal decomposition of PS nanobeads ($\phi = 100$ nm). In contrast, Coral $MoSe_2$-GC microspheres exhibited a relatively low BET surface area of 27 $m^2\ g^{-1}$ due to the absence of numerous surface defects caused by the PDA-derived N-doped C-coating layer (Fig. S9c). Moreover, the overall broad distribution of BJH pore size curves (Fig. S9d) indicates interconnected open pores, consistent with the FE-SEM image (Fig. 1b).

To demonstrate the structural advantages of Coral $MoSe_2$-GC@N—C microspheres, non-porous and carbon-free bare $MoSe_2$ powders were prepared as one of the comparison samples. The precursor microspheres obtained after spray pyrolysis exhibit spherical shape with smooth surface and no pores were observed throughout the structure (Fig. S10a and b). XRD pattern (Fig. S10c) displays the presence of various molybdenum oxide phases [Mo_4O_{11}, hexagonal MoO_3 (*h*-MoO_3), and orthorhombic MoO_3 (*α*-MoO_3)]. The obtained as-prepared MoO_x microspheres further underwent selenization at 500 ℃ to form bare $MoSe_2$ powders (Fig. S11). The low-resolution FE-SEM image (Fig. S11a) shows that the sample has a crumpled morphology with a non-uniform size distribution. Additionally, the FE-SEM image (Fig. S11b) reveals agglomerated sheet-type crystals, which is believed to be layered $MoSe_2$ flakes since carbon that can restrict the crystal growth during the selenization process was absent in bare $MoSe_2$. The TGA curve (Fig. S11c) confirms the absence of carbon in the bare $MoSe_2$ powder. The XRD pattern (Fig. S11d) demonstrates the complete phase transition from the MoO_x crystal phase to the 2H-$MoSe_2$ phase during the selenization. Moreover, the crystallite size of the bare $MoSe_2$ powder calculated through the Scherrer equation was 21 nm, which is significantly larger than that of the two samples (Coral $MoSe_2$-GC and Coral $MoSe_2$-GC@N—C). The N_2 adsorption–desorption isotherms (Fig. S11e) and the BJH desorption pore size distribution (Fig. S11f) indicate the presence of mesopores resulting from the crumpled $MoSe_2$ sheet, however the low BET surface area (4 $m^2\ g^{-1}$) suggests a negligible amount of pores. Additionally, a sharp peak at ~ 4 nm could be observed, which is attributed to the tensile-strength effect of N_2 desorption [56].

The electrochemical properties of 3D porous Coral $MoSe_2$-GC@N—C microspheres composited with GC and N-doped C coating on the surface are compared with Coral $MoSe_2$-GC microspheres and bare $MoSe_2$ as anodes for SIBs and shown in Fig. 4. The cyclic voltammetry (CV) curves corresponding to the three samples for the first 5 cycles obtained at a scan rate of 0.1 mV s^{-1} in the voltage range between 0.001 and 3.0 V are shown in Fig. 4a and S12. In the initial cathodic sweep, a broad peak at 1.03 V is identified, which corresponds to the formation of Na_xMoSe_2 phase due to the intercalation of Na-ions [18,21]. Two distinct peaks at 0.64 and 0.42 V are observed upon further sodiation, which respectively correspond to the conversion reaction, which resulted in the formation of metallic Mo and Na_2Se, and the formation of solid electrolyte interphase (SEI) layer resulting from the electrolyte decomposition [17,21]. A sharp peak at 1.73 V and a broad shoulder peak at 2.20 V, which can be observed during the initial charge process, correspond to the electrochemical reaction of Na_2Se and metallic Mo to form $MoSe_2$ phase and the formation of Na^+ and Se ($Na_2Se \rightarrow Se + 2Na^+ + 2e^-$), respectively [32,57,58]. From the second cycle, cathodic peaks at 1.81 and 1.36 V appeared, which correspond to the reaction of Se and Na to form Na_2Se phase and the conversion reaction of $MoSe_2$, respectively [59,60]. This explanation was in line with the ex-situ XRD pattern of Coral $MoSe_2$-GC@N—C electrode at different states of discharge and charge for the 1st and 2nd cycles (Fig. S13). The preselected potentials where the ex-situ analysis were carried out are depicted in Fig. S13a. For the initial state, $MoSe_2$ and 2H-$MoSe_2$ phases could be well observed, which is in agreement with the XRD pattern in Fig. 2h. In the initial discharge process, insertion of Na-ion led to the disappearance of (0 0 2) plane of

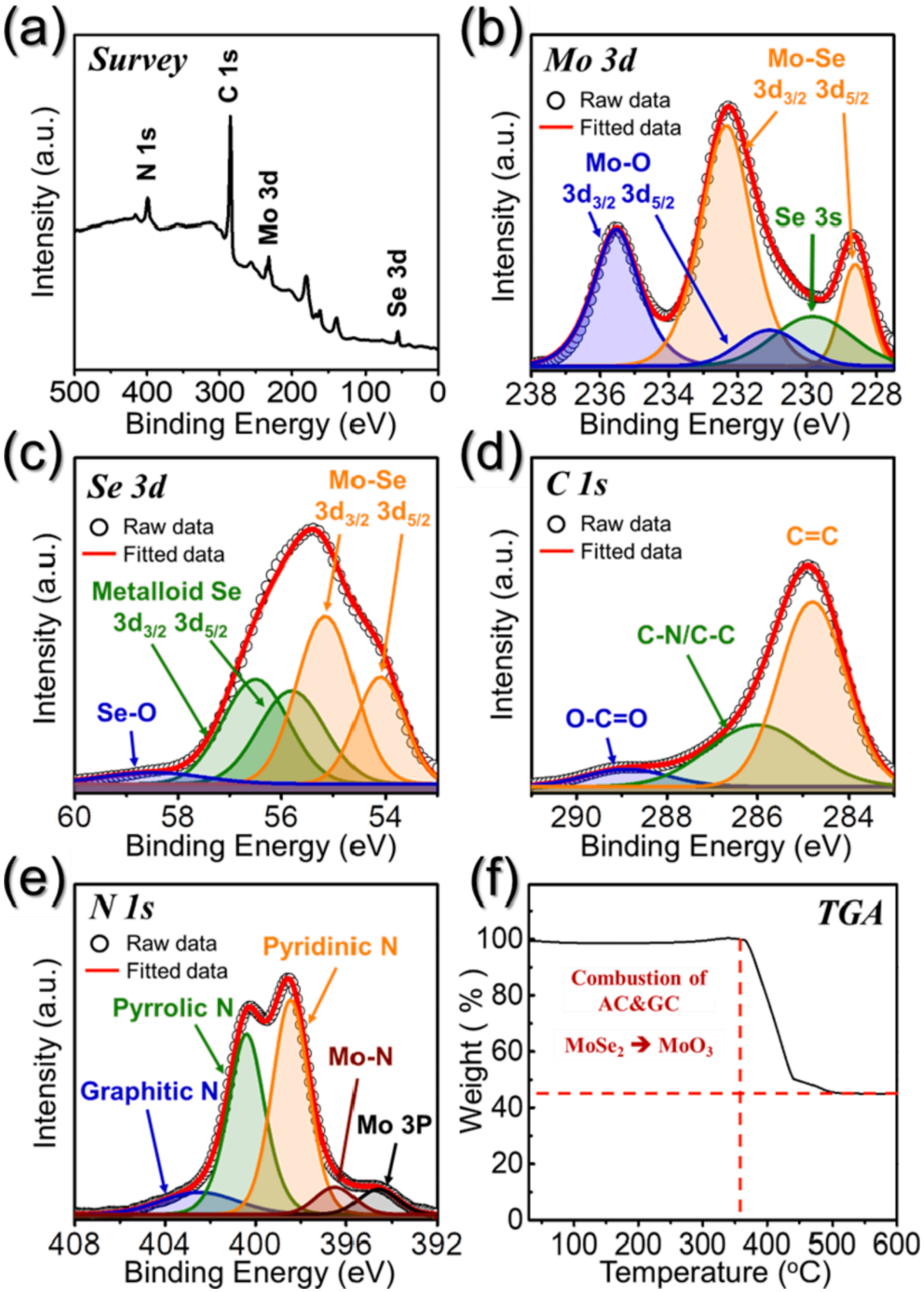

Fig. 3. XPS survey spectrum, core-level XPS spectra, and TG curve of Coral $MoSe_2$-GC@N—C composite microspheres: (a) XPS survey spectrum, (b) Mo 3d, (c) Se 3d, (d) C 1 s, (e) N 1 s, and (f) TG curve.

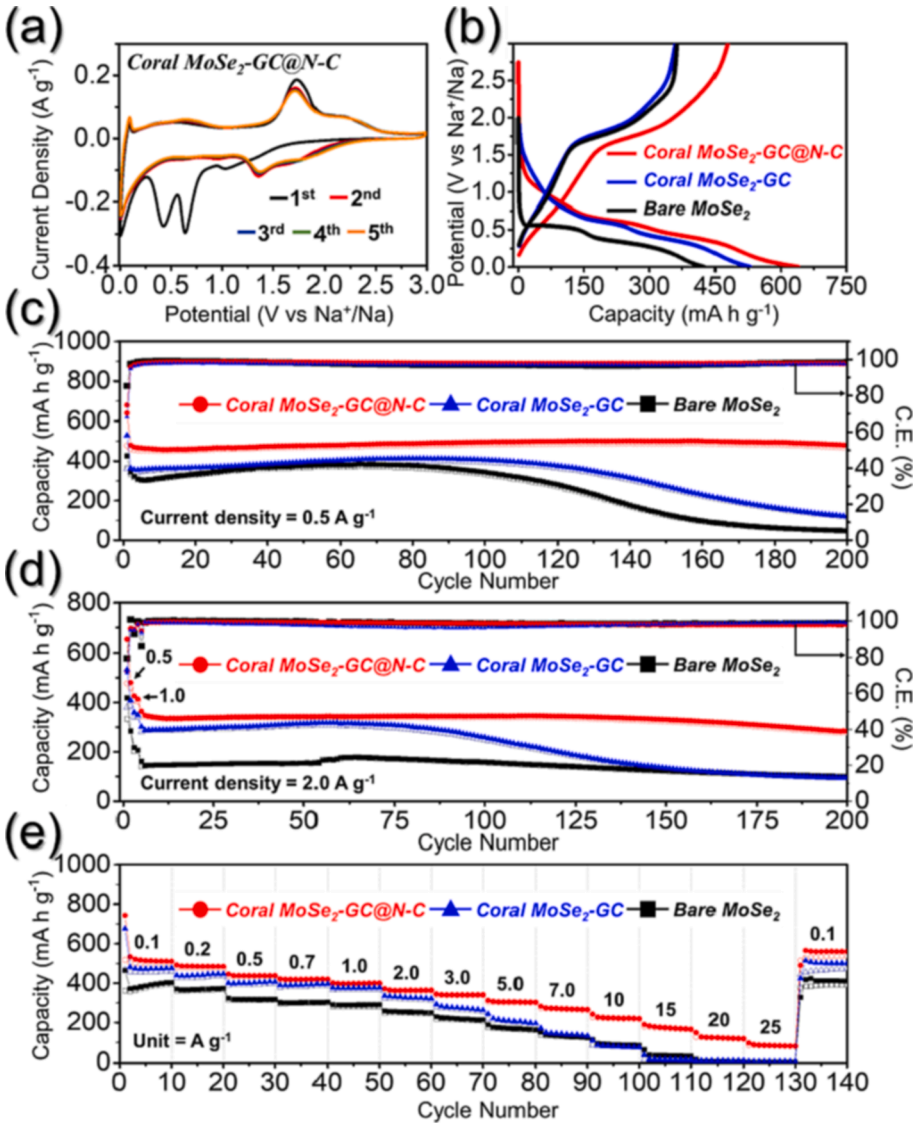

Fig. 4. Electrochemical properties of Coral $MoSe_2$-GC@N—C, Coral $MoSe_2$-GC, and bare $MoSe_2$ for Na-ion storage: (a) CV curve of Coral $MoSe_2$-GC@N—C microsphere, (b) initial discharge/charge curves at a constant current density of 0.5 A/g, (c) cycle performances at current density of 0.5 A/g, (d) cycle performances at current density of 2.0 A/g, and (e) rate performances.

molybdenum diselenide. When discharged to 0.9 V, peaks corresponding to 2H-$MoSe_2$ could be observed and further sodiation to 0.001 V resulted in the formation of Mo and Na_2Se phases. During the initial charge process, when charged up to 1.95 V, the reappearance of $MoSe_2$ could be identified and Na_2Se phase was also observed. When fully charged, peaks corresponding to $MoSe_2$ and Se were observed, and the presence of Se peak is attributed to the following electrochemical reaction: $Na_2Se \rightarrow Se + 2Na^+ + 2e^-$. In case of the second cycle, Mo and Na_2Se could be identified for the discharged state. The intensity of peaks corresponding to Na_2Se gradually decreased during charge process, and $MoSe_2$ and Se phases were observable for the fully charged state. The CV curves from the 2nd to 5th cycles overlapped well, which is indicative of the highly reversible redox reactions of Coral $MoSe_2$-GC@N—C microspheres. CV curves of Coral $MoSe_2$-GC microspheres and bare $MoSe_2$ were analogous to those of $MoSe_2$-GC@N—C microspheres, which is indicative of similar Na-ion storage mechanism (Fig. S12a and b). Notably, at potential near 0 V, Coral $MoSe_2$-GC@N—C microspheres exhibited a relatively sharper peak in comparison to the other two electrodes, which is attributed to the reaction of PDA-derived N-doped C with Na-ions [31]. For optimizing the electrochemical properties of Coral $MoSe_2$-GC@N—C microspheres, weight of PDA was controlled as shown in Fig. S14. Based on 100 mg of Coral $MoSe_2$-GC microspheres, 10, 50, and 100 mg of PDA were used for forming N-doped C shell. As can be expected, the thickness of carbon coating increased as the amount of PDA increased (Fig. S14(a-c)). The cycle performances of Coral $MoSe_2$-GC microspheres without PDA and with 10 mg, 50 mg, 100 mg PDA coating are shown in Fig. S14d. Rise in capacity could be observed with the increase in PDA amount up to 50 mg; the capacity was the highest for microspheres coated with 50 mg PDA. However, as the amount of PDA increased to 100 mg, capacity decreased to 366 mA h g^{-1}, which was even lower than $MoSe_2$-GC microspheres without PDA coating. In perspective of cycle stability, $MoSe_2$-GC microspheres (without PDA) exhibited gradual capacity degradation where 121 mA h g^{-1} was delivered after 200 cycles at 0.5 A g^{-1}. Microspheres coated with 10 mg PDA exhibited stable cycle performance up to 120th cycle but showed capacity fading afterwards. Microspheres with 50 and 100 mg PDA coating retained high capacities even after 200 cycles. Optimum amount of N-doped C derived from PDA coated on $MoSe_2$-GC microspheres allows the formation of 3D carbon network with high conductivity, leading to high capacity as well as stable cycle performance. 50 mg PDA was selected as the optimum coating amount since the anode exhibited the highest capacity as well as good capacity

retention.

The initial charge and discharge profiles of the microspheres obtained at a current density of 0.5 A g^{-1} are shown in Fig. 4b. The plateaus at which the electrochemical reactions occur were in line with the peak positions recorded in CV curves. In addition, difference in voltage hysteresis was observed; ΔV values for Coral $MoSe_2$-GC@N—C, Coral $MoSe_2$-GC microspheres, and bare $MoSe_2$ were 1.15, 1.47, and 1.60 V, respectively. (Fig. S15) Explicitly lower degree of polarization was observed in case of Coral $MoSe_2$-GC@N—C in comparison to the other samples since Na-ion diffusion was facilitated due to coating with N-doped C and GC surrounding the $MoSe_2$ particles, which resulted in high electrical conductivity. In addition, Coral $MoSe_2$-GC exhibited lower polarization in comparison to bare $MoSe_2$, which is attributed to the coral-like structures with numerous pores that enabled efficient electrolyte percolation and GC that increased electrical conductivity and redox kinetics. The initial discharge/charge capacities of Coral $MoSe_2$-GC@N—C, Coral $MoSe_2$-GC microspheres, and bare $MoSe_2$ were 640/478, 529/361, and 426/363 mA h g^{-1}, respectively (Fig. 4b). The initial Coulombic efficiencies (ICE) of the samples were 74.7 %, 68.2 %, and 85.2 %, respectively; Coral $MoSe_2$-GC@N—C and Coral $MoSe_2$-GC microspheres exhibited relatively lower ICEs than bare $MoSe_2$ since they were composited with carbon material with low ICE. However, Coral $MoSe_2$-GC@N—C microspheres exhibited higher ICEs in comparison to Coral $MoSe_2$-GC microspheres although Coral $MoSe_2$-GC@N—C has higher amount of C content (15.9 wt%) than Coral $MoSe_2$-GC (5.2 wt%), which is attributed to the N-doped C layer that enhanced the electrical conductivity and reduced some irreversible reactions. Coral $MoSe_2$-GC@N—C microspheres exhibited a relatively long slopy lines near 0 V (Fig. 4b), which is attributed to the reaction of N-doped C with Na-ions, leading to higher capacities. The cycle performances of Coral $MoSe_2$-GC@N—C, Coral $MoSe_2$-GC microspheres, and bare $MoSe_2$ as anodes for SIBs at a current density of 0.5 A g^{-1} are shown in Fig. 4c. Coral $MoSe_2$-GC@N—C exhibited stable cycle performance up to the 200th cycle, where a reversible capacity of 479 mA h g^{-1} was delivered. This could be attributed to the N-doped C coating and the interconnected 3D porous structure that effectively alleviated the volume changes that occur during repetitive charge and discharge processes. Coral $MoSe_2$-GC microspheres exhibited higher structural robustness in comparison to bare $MoSe_2$, which again verifies the role of 3D porous structure in effectively enduring the volume changes during cycling. In addition, the cycle performances of the samples were tested at current densities of 0.5 and 1.0 A g^{-1} for two cycles each and at 2.0 A g^{-1} up to 200th cycle (Fig. 4d). Due to the structural merits, Coral $MoSe_2$-GC@N—C retained high capacity of 284 mA h g^{-1}, which is approximately 2.8 times higher in comparison to the other two. The rate performances of the microspheres were tested at current densities ranging from 0.1 to 25 A g^{-1}, and the results are provided in Fig. 4e. In case of Coral $MoSe_2$-GC@N—C microspheres, capacities of 511, 484, 438, 420, 400, 365, 341, 304, 267, 221, 167, 119, and 82 mA h g^{-1} were recorded at current densities of 0.1, 0.2, 0.5, 0.7, 1.0, 2.0, 3.0, 5.0, 7.0, 10, 15, 20, and 25 A g^{-1}, respectively. When the current density returned to 0.1 A g^{-1}, the capacity was well-recovered to 565 mA h g^{-1}. Explicit difference between the capacities of Coral $MoSe_2$-GC@N—C and Coral $MoSe_2$-GC microspheres could be observed at current densities higher than 3.0 A g^{-1}. Capacities of Coral $MoSe_2$-GC microspheres decreased from 467 to 5 mA h g^{-1} when the current density increased from 0.1 to 25 A g^{-1}. Bare $MoSe_2$ exhibited the lowest capacities among the three samples at almost all current densities. The superior rate capability of Coral $MoSe_2$-GC@N—C in comparison to Coral $MoSe_2$-GC microspheres and bare $MoSe_2$ derived from the interconnected 3D porous structure, which enabled easy penetration of electrolyte as well as decreased the ion diffusion path. In addition, N-doped C coating on the surface with high electrical conductivity accelerated the electrochemical kinetics of the anode. GC in the microspheres has also acted as the matrix that supplemented electrical conductivity. Owing to these structural merits, Coral $MoSe_2$-GC@N—C exhibited superior electrochemical properties with various $MoSe_2$ materials applied as anodes for SIBs (Table S2). Moreover, to explore the potential of Coral $MoSe_2$-GC@N—C anode for practical use, it was coupled with $Na_3V_2(PO_4)_3$/carbon microspheres prepared from the spray drying process for preparation of sodium-ion full cell, and the relevant information is provided in Fig. S16 and S17.

To explain the origin of the fast Na-ion storage kinetics of Coral $MoSe_2$-GC@N—C, CV curves of three samples were obtained at sweep rates ranging from 0.1 to 2.0 mV s^{-1} and are presented in Fig. 5a, S18a and c. The power law, $i = av^b$, was applied to obtain *b*-values, which can be used to understand whether the electrochemical reaction is surface-capacitive or diffusion-limited [61,62]. *b*-value close to unity indicates that the reaction is dominated by surface-capacitive reaction whereas that close to 0.5 implies that the electrochemical reaction is diffusion-controlled [61–64]. *b*-values were calculated for Peaks 1 ~ 4 at which the main redox reactions occur using the relationship between log (*i*) vs log (*v*) and are shown in Fig. 5b, S18b, and d. *b*-values of Coral $MoSe_2$-GC@N—C for Peaks 1 ~ 4 were 0.97, 0.92, 0.90, and 0.94, which were larger than Coral $MoSe_2$-GC microspheres due to the successful coating of N-doped C layer with relatively higher electrical conductivity. Coral $MoSe_2$-GC microspheres exhibited higher b-values in comparison to bare $MoSe_2$ probably due to the interconnected porous network that effectively reduced the Na-ion diffusion length and enhanced the contact between electrode and electrolyte, leading to higher degree of surface-capacitive reactions. In addition, the amount of surface-capacitive reaction and the diffusion-controlled reaction was quantitatively distinguished using the following equation: $i = k_1v + k_2v^{1/2}$ [57,62]. The former corresponds to the current derived from surface-capacitive reaction whereas the latter indicates the current from diffusion-controlled reaction. The percentages of capacitive reactions in comparison to the empirically obtained current for Coral $MoSe_2$-GC@N—C, Coral $MoSe_2$-GC microspheres, and bare $MoSe_2$ at scan rate of 2.0 mV s^{-1} were 90, 88, and 70 % (Fig. 5c, e, and g), respectively. The percentage of capacitive contribution at various scan rates from 0.1 to 2.0 mV s^{-1} are summarized in Fig. 5d, f, and h. The large difference between microspheres with coral structure and dense structure is attributed to the 3D interconnected porous network, which facilitated the surface-capacitive reactions as well as enhanced the contact area between electrode and electrolyte. In addition, Coral $MoSe_2$-GC@N—C exhibited higher capacitive contribution in comparison to Coral $MoSe_2$-GC, which is due to the N-doped C matrix that successfully encompassed $MoSe_2$ microspheres and provided additional electrical conductivity.

The stable and fast Na-ion storage capabilities of Coral $MoSe_2$-GC@N—C microspheres in comparison to those of Coral $MoSe_2$-GC microspheres and bare $MoSe_2$ were confirmed with the electrochemical impedance spectroscopy (Fig. 6). The Nyquist plots of the electrode materials were obtained prior to cycling, and after the 1st and 100th cycles at the fully charged states. The obtained Nyquist plots were further deconvoluted with the Randles-type equivalent circuit shown in Fig. S19. Charge transfer resistance (R_{ct}) of Coral $MoSe_2$-GC@N—C, Coral $MoSe_2$-GC microspheres, and bare $MoSe_2$ for the freshly assembled cells were 158, 314, and 404 Ω, respectively (Fig. 6a). Coral $MoSe_2$-GC microspheres exhibited lower R_{ct} in comparison to bare $MoSe_2$ due to the presence of GC with relatively higher electrical conductivity. When coated with N-doped C on the surface which enabled high electrical conductivity, drastic decrease in R_{ct} was observed, indicating the enhanced charge transfer kinetics. After the 1st cycle, R_{ct} values of all electrodes decreased, which is attributed to the formation of ultrafine nanocrystals (Fig. 6b) [65,66]. The Nyquist plots of the electrodes after the 100th cycle are presented in Fig. 6c, where Coral $MoSe_2$-GC@N—C, Coral $MoSe_2$-GC microspheres, and bare $MoSe_2$ exhibited R_{ct} values of 65, 109, and 155 Ω, respectively. The SEM images of the electrode materials were taken after 150 cycles at 0.5 A g^{-1} (Fig. 6(d-f)) to understand the difference in R_{ct} values between the microspheres. R_{ct} of Coral $MoSe_2$-GC@N—C was very low in comparison to the other microspheres, which is due to the structural robustness arising from N-

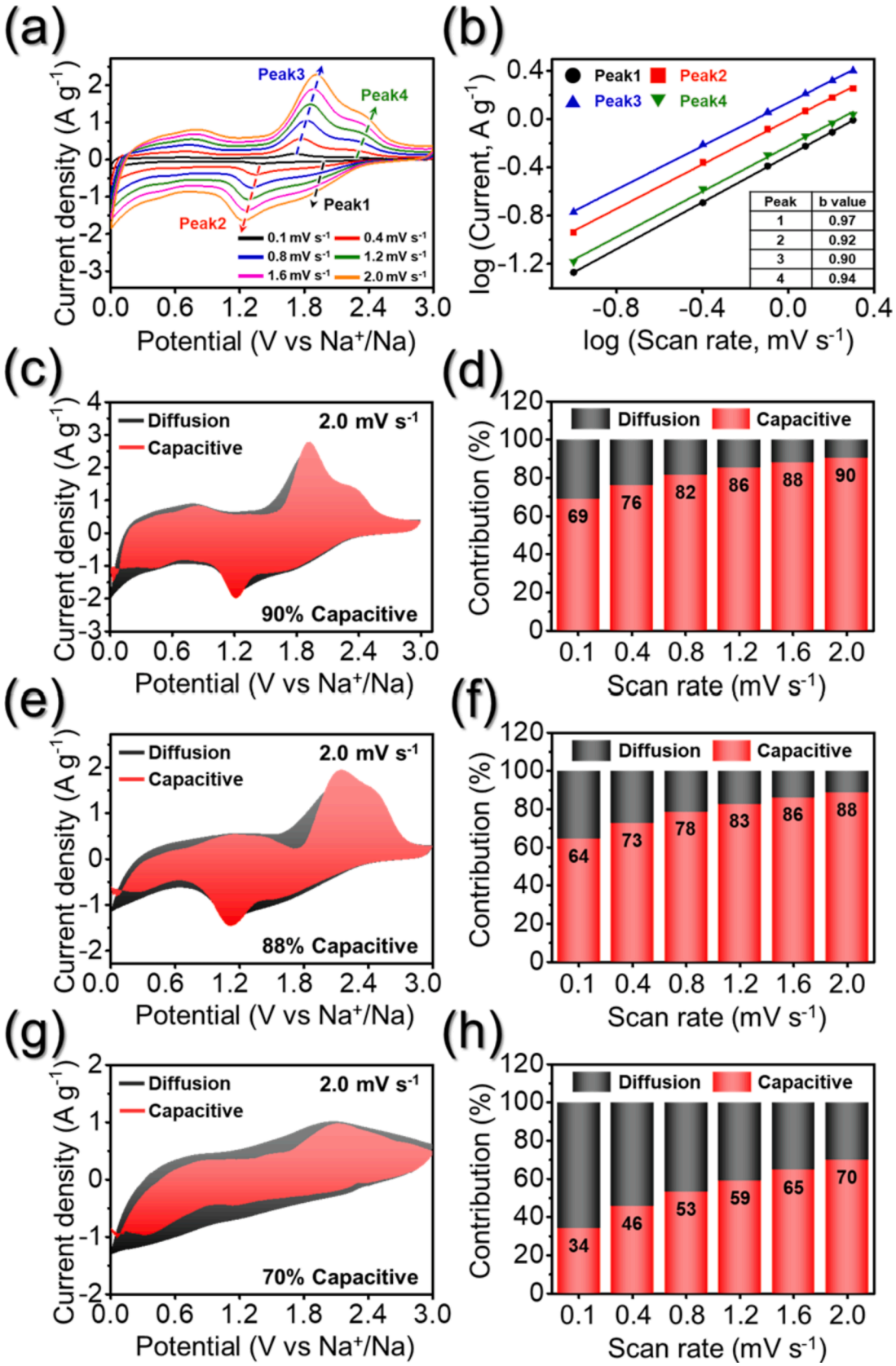

Fig. 5. Electrochemical reaction dynamics analysis of (a-d) the Coral $MoSe_2$-GC@N—C, (e,f) Coral $MoSe_2$-GC, and (g,h) bare $MoSe_2$ for Na-ion storage: (a) CV curves obtained at various scan rates, (b) current response (*i*) versus scan rate (*n*) at each redox peak, (c,e,g) CV curves with the capacitive fraction shown by the red region at a scan rate of 2.0 m V s^{-1}, and (d,f,h) bar chart showing the percentage of the capacitive contribution at different scan rates.

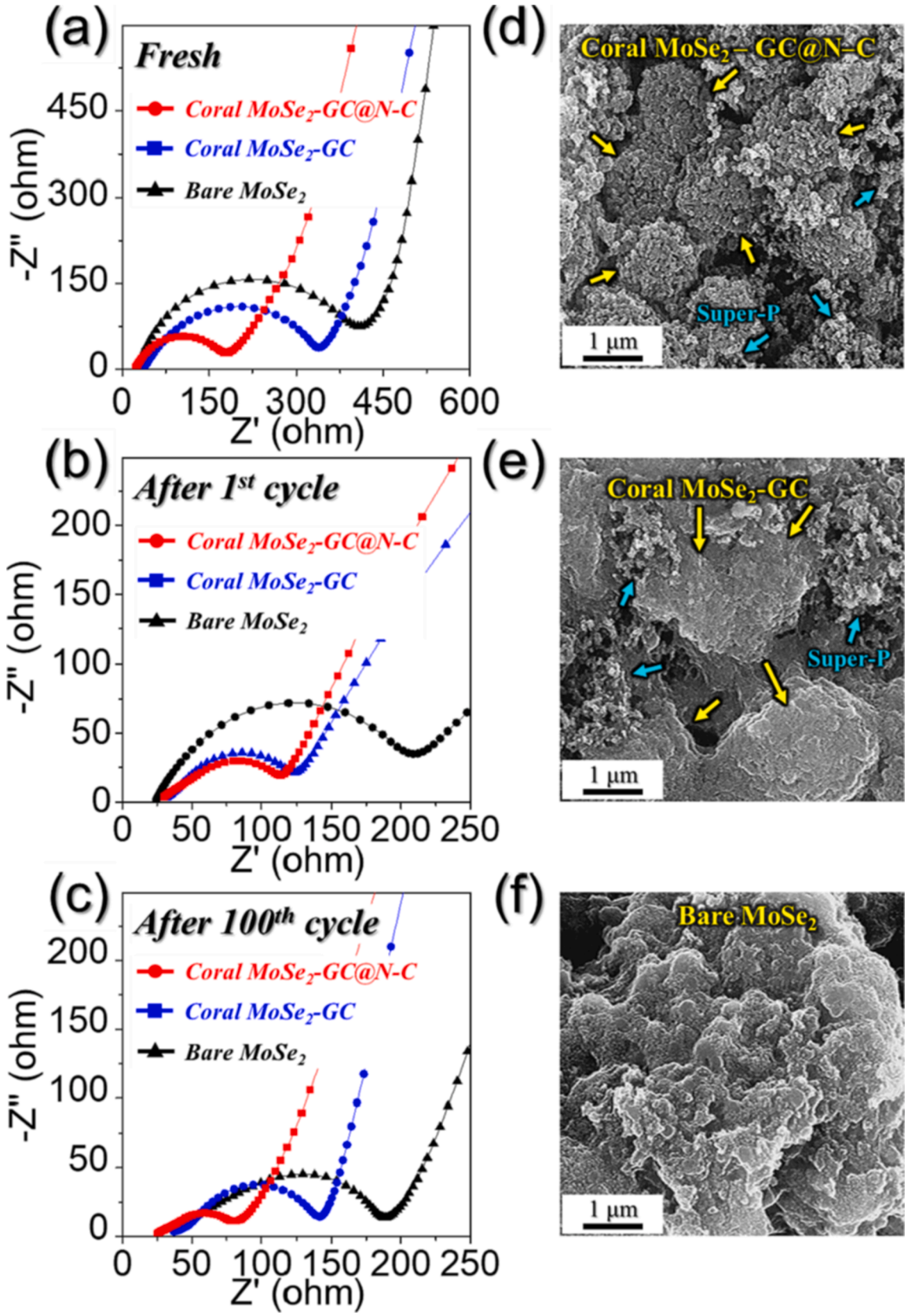

Fig. 6. (a-c) Nyquist impedance plots and (d-f) FE-SEM images of the Coral $MoSe_2$-GC@N—C, Coral $MoSe_2$-GC, bare $MoSe_2$ obtained after 150th cycles at 0.5 A g^{-1} for Na-ion storage: (a) before cycling, (b) after 1st cycle, (c) after 100th cycle, (d) the Coral $MoSe_2$-GC@N—C, (e) Coral $MoSe_2$-GC, and (f) bare $MoSe_2$.

doped C coating as can be ascertained with the SEM image in Fig. 6d. Coral $MoSe_2$-GC microspheres suffered from structural degradation to some degree during repetitive cycling as shown in Fig. 6e, which resulted in much higher R_{ct} than N-doped C-coated counterpart. Bare $MoSe_2$ could not withstand the stress induced during cycling, which led to the formation of bulky agglomerates, which resulted in the highest R_{ct} after 150 cycles among the three microspheres (Fig. 6f).

The structural merits of Coral $MoSe_2$-GC@N—C microspheres that lead to high electrochemical kinetics were further ascertained by applying Randle-Sevcik equation: $I_p = 0.4463nFAC(nFnD/RT)^{1/2} = [(269,000)n^{3/2}AD^{1/2}C]v^{1/2}$ (Fig. 7) whose parameters are well described in the previous work [67]. In our case, n, A, and C correspond to 4, 1.5386 cm^2, and 0.001 mol cm^{-3}, respectively. The Peaks for which the Na-ion diffusivity is calculated are shown in Fig. 7(a-c). The linear relationship between peak current (V) and square root of scan rate ($v^{1/2}$) are presented in Fig. 7(d-f); the Na-ion diffusivity of Coral $MoSe_2$-GC@N—C, Coral $MoSe_2$-GC microspheres, and bare $MoSe_2$ is summarized in Fig. 7g. Diffusivity of Coral $MoSe_2$-GC microspheres was explicitly higher than that of bare $MoSe_2$, which is attributed to the 3D interconnected porous structure and presence of GC that facilitated the diffusion of Na-ions. Coral $MoSe_2$-GC@N—C microspheres with N-doped C matrix with high electrical conductivity and coral-like structure exhibited the highest diffusivity for all peaks. The calculation results can well explain the origin of fast Na-ion storage kinetics in Coral $MoSe_2$-GC@N—C microspheres, which led to high capacities even at a high charging rate of 25 A g^{-1}.

The electrochemical properties of Coral $MoSe_2$-GC@N—C, Coral $MoSe_2$-GC microspheres, and bare $MoSe_2$ as anodes for PIBs are presented in Fig. 8. CV curves of Coral $MoSe_2$-GC@N—C microspheres were recorded at a sweep rate of 0.1 mV s^{-1} and are presented in Fig. 8a. During initial discharge process, reaction between $MoSe_2$ and K-ions occurred, resulting in the formation of K_xMoSe_2 [68–70]. The distinct peak that appears at 0.25 V corresponds to the conversion reaction that results in the formation of Mo and K_2Se phases as well as the formation of SEI layer [68–70]. During the charge process, peak relevant to the formation of $MoSe_2$ material could be found at 1.7 V [68,70]. From the second cycle and on, during discharge process, a distinct peak corresponding to the transformation of $MoSe_2$ into Mo and K_2Se could be observed at 1.1 V [53,68]. Reversible conversion reaction that leads to the formation of $MoSe_2$ could be observed at 1.7 V during the anodic sweep [53,68,70]. The CV curves overlapped well from the second cycle, which is indicative of highly reversible redox reactions. The CV curves for Coral $MoSe_2$-GC microspheres and bare $MoSe_2$ are also provided in Fig. S20, which exhibited similar shapes with that of Coral $MoSe_2$-GC@N—C microspheres. The initial charge–discharge profiles of the anodes recorded at a current density of 1.0 A g^{-1} are shown in Fig. 8b; Coral $MoSe_2$-GC@N—C, Coral $MoSe_2$-GC microspheres, and bare $MoSe_2$ exhibited discharge capacities of 417, 408, and 294 mA h g^{-1}, with Coulombic efficiencies of 66, 73 and 72 %, respectively. Notably, in case of K-ion storage, Coral $MoSe_2$-GC@N—C microspheres didn't exhibit higher capacities in comparison to Coral $MoSe_2$-GC microspheres, which is in contrast to the results of SIBs. The charge–discharge profiles in Fig. 8b didn't exhibit a slopy line at potential near 0 V, which is in line with the results of CV analysis in Fig. 8a. This implies that K-ions only go through pseudocapacitive electrochemical reactions at N-doped C's surface; therefore, capacity increase effect by N-doped C coating was not observed. The cycle performances of the three electrodes were tested at a current density of 1.0 A g^{-1}, where Coral $MoSe_2$-GC@N—C microspheres exhibited high structural integrity; a capacity of 251 mA h g^{-1} could be delivered even after 150 cycles (Fig. 8c). The structural merits of Coral $MoSe_2$-GC@N—C microspheres also led to the stable cycle performances as anode for PIBs. Coral $MoSe_2$-GC microspheres exhibited higher capacities in comparison to bare $MoSe_2$ at 1.0 A g^{-1}, which is attributed to the 3D porous structure that led to rich redox reactions and enlarged active areas. Since N-doped C shielding was not present in Coral $MoSe_2$-GC microspheres, stress received during repetitive cycling

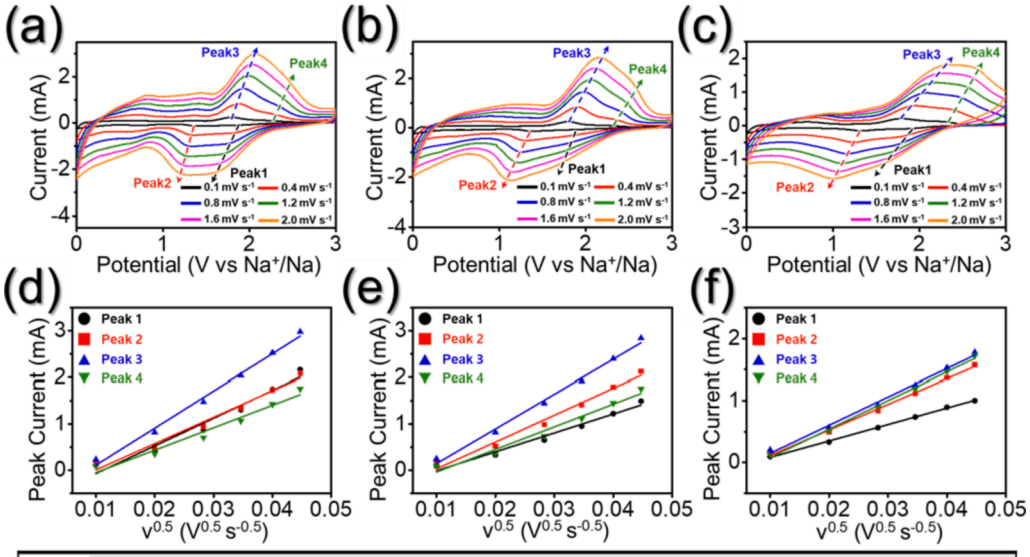

(g)

Sample	D_{Na^+} (cm^2 s^{-1}) × 10^{-10}				Avg. D_{Na^+} (cm^2 s^{-1}) × 10^{-10}
	Peak 1	Peak 2	Peak 3	Peak 4	
Coral $MoSe_2$-GC@N-C	3.27	2.96	5.83	2.15	3.55
Coral $MoSe_2$-GC	1.53	3.07	5.12	2.18	2.98
Bare $MoSe_2$	0.65	1.56	1.90	1.94	1.51

Fig. 7. Na-ion diffusion coefficient (D_{Na^+}) for the SIB: (a,d) Coral $MoSe_2$-GC@N—C, (b,e) Coral $MoSe_2$-GC, (c,f) bare $MoSe_2$, and (g) Na-ion diffusion coefficient comparison table.

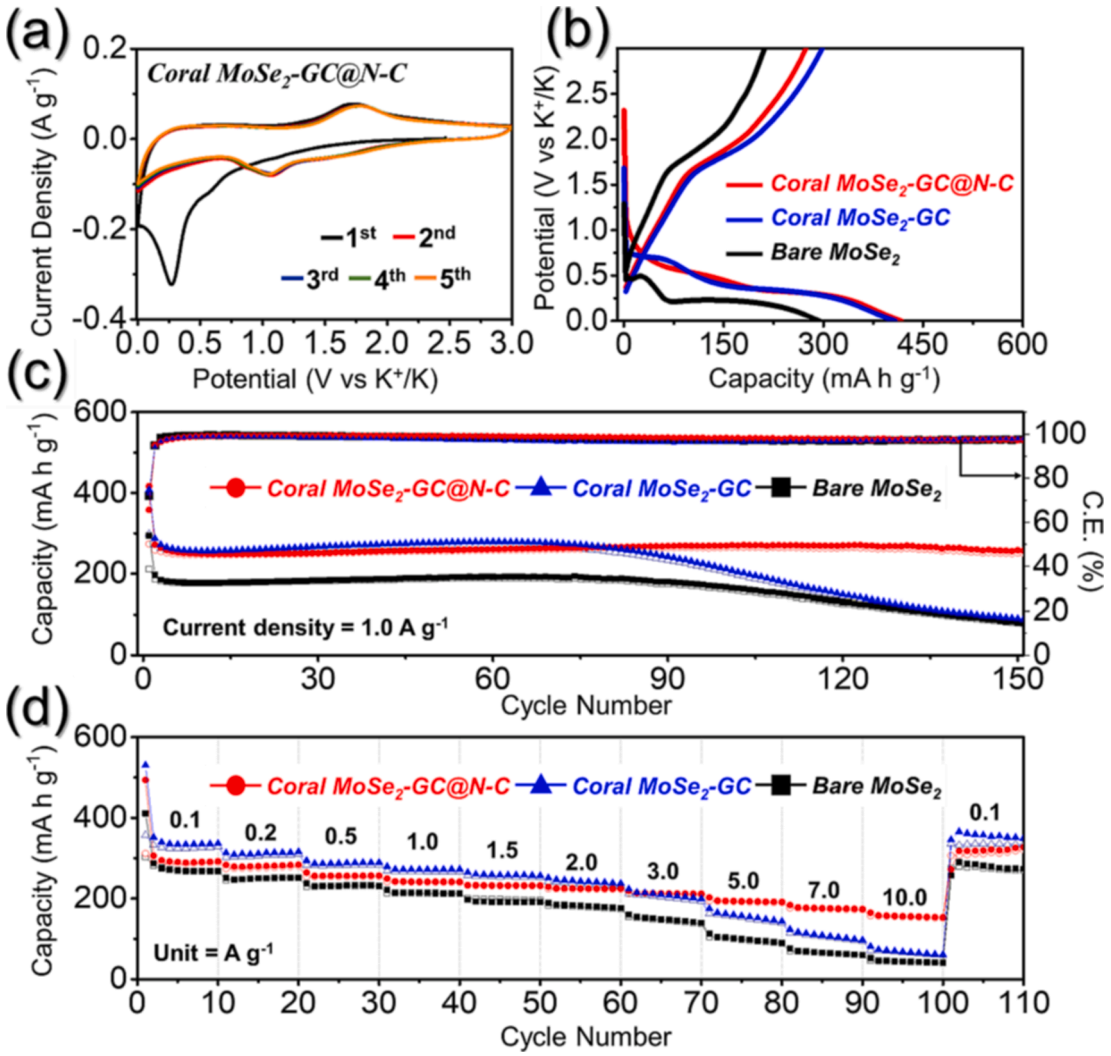

Fig. 8. Electrochemical properties of Coral $MoSe_2$-GC@N—C, Coral $MoSe_2$-GC, and bare $MoSe_2$ for K-ion storage: (a) CV curve of coral $MoSe_2$-GC@N—C microsphere, (b) initial discharge/charge curves at a constant current density of 1.0 A/g, (c) cycle performances at current density of 1.0 A/g, and (d) rate performances.

was not effectively alleviated, leading to capacity degradation at cycle number over 70th. The rate performances of the three electrodes tested at current densities ranging from 0.1 to 10.0 A g^{-1} are presented in Fig. 8d. In case of Coral $MoSe_2$-GC@N—C microspheres, capacities of 290, 280, 254, 240, 231, 223, 210, 190, 172, and 152 mA h g^{-1} were recorded at current densities of 0.1, 0.2, 0.5, 1.0, 1.5, 2.0, 3.0, 5.0, 7.0, and 10 A g^{-1}, respectively. In comparison, the capacities of Coral $MoSe_2$-GC microspheres and bare $MoSe_2$ decreased from 328 and 60 mA h g^{-1} to 269 and 41 mA h g^{-1}, respectively, when the current density changed from 0.1 to 10 A g^{-1}. The strategy of introducing interconnected 3D porous structure as well as conductive N-doped C coating at the surface led to great performances even when applied as anode for PIBs. The electrochemical properties of various nanostructured $MoSe_2$ materials applied as anode for PIBs are presented in Table S3; Coral $MoSe_2$-GC@N—C microspheres exhibited high performance, especially in terms of rate capability.

The origin of the fast electrochemical kinetics of Coral $MoSe_2$-GC@N—C microspheres, which enabled high capacity of 152 mA h g^{-1} at 10 A g^{-1}, was unveiled by obtaining CV curves at various scan rates (Fig. S21a). *b*-values obtained from the relationship between log (*i*) vs log (*v*) for Peaks 1 ~ 3 were 1.00, 0.80, and 0.97, indicating high degree of surface capacitive reaction (Fig. S21b). Furthermore, Coral $MoSe_2$-GC@N—C microspheres showed 90 % surface-capacitive reaction at a scan rate of 1.2 mV s^{-1} (Fig. S21c). The bar chart indicating the percentage of capacitive contribution at various scan rates is shown in Fig. S21d, where the percentage increased from 62 % to 90 % when the scan rate increased from 0.1 to 1.2 mV s^{-1}. The electrochemical impedance spectroscopy (EIS) analyses of Coral $MoSe_2$-GC@N—C, Coral $MoSe_2$-GC microspheres, and bare $MoSe_2$ for the K-ion storage prior to cycling and for the 1st, 10th, and 150th cycles are shown in Fig. S22. For the freshly assembled cells, Coral $MoSe_2$-GC@N—C exhibited the lowest R_{ct}, followed by Coral $MoSe_2$-GC microspheres and bare $MoSe_2$, which was in line with the EIS results for the sodium counterpart (Fig. 6). The trend could also be observed in the Nyquist plots for the 1st, 10th and 150th cycle. R_{ct} values of Coral $MoSe_2$-GC@N—C, Coral $MoSe_2$-GC microspheres, and bare $MoSe_2$ for the 150th cycle were 1578, 2416, and 4715 Ω, respectively. The SEM images of the microspheres after 150 cycles at 1.0 A g^{-1} are presented in Fig. S22(e-g). The spherical morphology of Coral $MoSe_2$-GC@N—C microspheres were well retained even after 150 cycles, which can explain why the R_{ct} values for the 10th and 150th cycles were similar. Coral $MoSe_2$-GC microspheres experienced some structure destruction during repetitive cycles, leading to an increase in R_{ct}. The structure of bare $MoSe_2$ was completely collapsed during cycling and formed bulky agglomerates, which resulted in very high R_{ct} value after 150 cycles. Overall, the results suggest that Coral $MoSe_2$-GC@N—C microspheres characterized by 3D interconnected pore structure composited with GC, to which PDA-derived N-doped C is coated provides high structural integrity and electrical conductivity,

which led to high electrochemical properties when applied as anodes for both SIBs and PIBs.

4. Conclusions

In this study, coral-like porous microspheres comprising PDA-derived N-doped C-coated $MoSe_2$ composited with GC (Coral $MoSe_2$-GC@N—C) were prepared from a facile spray pyrolysis process, selenization heat-treatment, and subsequent N-doped C coating. The 3D interconnected porous microspheres effectively alleviated the volume changes and allowed facile penetration of the electrolyte into the nanostructure. Small-sized $MoSe_2$ nanosheets with enlarged interlayer spacing composited with GC were further coated with N-doped C, which enabled rapid transfer of electrons through dual carbon coating configuration, leading to fast redox kinetics. Owing to these features, when applied as anodes for both SIBs and PIBs, the microspheres exhibited structural robustness and high rate capability. In particular, the anode could deliver high capacities at current densities of 25 A/g and 10 A/g for SIBs and PIBs, which well demonstrates that this strategy is advantageous in achieving good electrochemical properties at high charging rate. This strategy may pave the way towards the development of 3D porous microspheres with desired composition coated with conductive carbon matrix for various energy-related applications.

Declaration of Competing Interest

The authors declare that they have no known competing financial interests or personal relationships that could have appeared to influence the work reported in this paper.

Data availability

No data was used for the research described in the article.

Acknowledgments

This work was supported by the National Research Foundation of Korea (NRF) grant funded by the Korean government (MSIP) (No. NRF-2021R1A4A2001687, and NRF-2021R1I1A3057700. This work was partly supported by Korea Institute of Energy Technology Evaluation and Planning (KETEP) grant funded by the Korea government (MOTIE) (20224000000070, Human Resource Training for Smart Energy New Industry Cluster).

Appendix A. Supplementary data

Supplementary data to this article can be found online at https://doi.org/10.1016/j.cej.2022.141118.

References

[1] K. Kubota, M. Dahbi, T. Hosaka, S. Kumakura, S. Komaba, Towards K-ion and Na-ion batteries as “beyond Li-ion”, Chem. Rec. 18 (2018) 459–479, https://doi.org/10.1002/tcr.201700057.
[2] R. Rajagopalan, Y. Tang, X. Ji, C. Jia, H. Wang, Advancements and challenges in potassium ion batteries: A comprehensive review, Adv. Funct. Mater. 30 (2020) 1909486, https://doi.org/10.1002/adfm.201909486.
[3] B. Sun, P. Li, J. Zhang, D. Wang, P. Munroe, C. Wang, P.H. Notten, G. Wang, Dendrite-free sodium-metal anodes for high-energy sodium-metal batteries, Adv. Mater. 30 (2018) 1801334, https://doi.org/10.1002/adma.201801334.
[4] J. Sun, H.-W. Lee, M. Pasta, H. Yuan, G. Zheng, Y. Sun, Y. Li, Y. Cui, A phosphorene–graphene hybrid material as a high-capacity anode for sodium-ion batteries, Nat. Nanotechnol. 10 (2015) 980–985, https://doi.org/10.1038/nnano.2015.194.
[5] H. Yang, R. Xu, Y. Yao, S. Ye, X. Zhou, Y. Yu, Multicore–shell Bi@N-doped carbon nanospheres for high power density and long cycle life sodium- and potassium-ion anodes, Adv. Funct. Mater. 29 (2019) 1809195, https://doi.org/10.1002/adfm.201809195.
[6] L. Ma, Y. Lv, J. Wu, C. Xia, Q. Kang, Y. Zhang, H. Liang, Z. Jin, Recent advances in anode materials for potassium-ion batteries: A review, Nano Res. 14 (2021) 4442–4470, https://doi.org/10.1007/s12274-021-3439-3.
[7] K. Song, C. Liu, L. Mi, S. Chou, W. Chen, C. Shen, Recent progress on the alloy-based anode for sodium-ion batteries and potassium-ion batteries, Small 17 (2021) 1903194, https://doi.org/10.1002/smll.201903194.
[8] J.S. Cho, S.Y. Lee, J.-K. Lee, Y.C. Kang, Iron telluride-decorated reduced graphene oxide hybrid microspheres as anode materials with improved Na-ion storage properties, ACS Appl. Mater. Interfaces 8 (2016) 21343–21349, https://doi.org/10.1021/acsami.6b05758.
[9] Y. Zhu, X. Han, Y. Xu, Y. Liu, S. Zheng, K. Xu, L. Hu, C. Wang, Electrospun Sb/C fibers for a stable and fast sodium-ion battery anode, ACS Nano 7 (2013) 6378–6386, https://doi.org/10.1021/nn4025674.
[10] D. Chao, P. Liang, Z. Chen, L. Bai, H. Shen, X. Liu, X. Xia, Y. Zhao, S.V. Savilov, J. Lin, Pseudocapacitive Na-ion storage boosts high rate and areal capacity of self-branched 2D layered metal chalcogenide nanoarrays, ACS Nano 10 (2016) 10211–10219, https://doi.org/10.1021/acsnano.6b05566.
[11] J.S. Cho, H.S. Ju, J.-K. Lee, Y.C. Kang, Carbon/two-dimensional $MoTe_2$ core/shell-structured microspheres as an anode material for Na-ion batteries, Nanoscale 9 (2017) 1942–1950, https://doi.org/10.1039/C6NR07158A.
[12] H. Tian, X. Yu, H. Shao, L. Dong, Y. Chen, X. Fang, C. Wang, W. Han, G. Wang, Unlocking few-layered ternary chalcogenides for high-performance potassium-ion storage, Adv. Energy Mater. 9 (2019) 1901560, https://doi.org/10.1002/aenm.201901560.
[13] C. Zhang, H. Zhao, Y. Lei, Recent research progress of anode materials for potassium-ion batteries, Energy Environ. Mater. 3 (2020) 105–120, https://doi.org/10.1002/eem2.12059.
[14] H.H. Lu, C.S. Shi, N.Q. Zhao, E.Z. Liu, C.N. He, F. He, Carbon and few-layer MoS_2 nanosheets co-modified TiO_2 nanosheets with enhanced electrochemical properties for lithium storage, Rare Met. 37 (2018) 107–117, https://doi.org/10.1007/s12598-017-0983-9.
[15] H. Fan, P. Mao, G. Lan, C. Liu, J. Chen, Z. Wang, Z. Li, R. Zheng, Y. Liu, H. Sun, Ultrathin metallic-phase molybdenum disulfide nanosheets stabilized on functionalized carbon nanotubes via covalent interface interaction for sodium-and lithium-ion storage, ACS Appl. Energy Mater. 4 (2021) 9440–9449, https://doi.org/10.1021/acsaem.1c01638.
[16] R. Pothu, R. Bolagam, Q.H. Wang, W. Ni, J.-F. Cai, X.-X. Peng, Y.-Z. Feng, J.-M. Ma, Nickel sulfide-based energy storage materials for high-performance electrochemical capacitors, Rare Met. 40 (2021) 353–373, https://doi.org/10.1007/s12598-020-01470-w.
[17] S.Y. Jeong, S.-K. Park, Y.C. Kang, J.S. Cho, One-dimensional nanostructure comprising $MoSe_2$ nanosheets and carbon with uniformly defined nanovoids as an anode for high-performance sodium-ion batteries, Chem. Eng. J. 351 (2018) 559–568, https://doi.org/10.1016/j.cej.2018.06.130.
[18] G.D. Park, J.H. Kim, S.-K. Park, Y.C. Kang, $MoSe_2$ embedded CNT-reduced graphene oxide composite microsphere with superior sodium ion storage and electrocatalytic hydrogen evolution performances, ACS Appl. Mater. Interfaces 9 (2017) 10673–10683, https://doi.org/10.1021/acsami.7b00147.
[19] Y.H. Seon, Y.C. Kang, J.S. Cho, One-dimensional porous nanostructure composed of few-layered $MoSe_2$ nanosheets and highly densified-entangled-N-doped CNTs as anodes for Na ion batteries, Chem. Eng. J. 425 (2021), 129051, https://doi.org/10.1016/j.cej.2021.129051.
[20] X. Zhang, Y. Xiong, M. Dong, Z. Hou, Y. Qian, Construction of hierarchical $MoSe_2$@C hollow nanospheres for efficient lithium/sodium ion storage, Inorg. Chem. Front. 7 (2020) 1691–1698, https://doi.org/10.1039/D0QI00017E.
[21] Y. Tang, Z. Zhao, Y. Wang, Y. Dong, Y. Liu, X. Wang, J. Qiu, Carbon-stabilized interlayer-expanded few-layer $MoSe_2$ nanosheets for sodium ion batteries with enhanced rate capability and cycling performance, ACS Appl. Mater. Interfaces 8 (2016) 32324–32332, https://doi.org/10.1021/acsami.6b11230.
[22] J.S. Lee, R. Saroha, S.H. Oh, D.H. Shin, S.M. Jeong, J.K. Kim, J.S. Cho, Rational design of perforated bimetallic (Ni, Mo) sulfides/N-doped graphitic carbon composite microspheres as anode materials for superior Na-ion batteries, Small Methods 5 (2021) 2100195, https://doi.org/10.1002/smtd.202100195.
[23] S. Liang, H. Shi, Z. Yu, Q. Liu, K. Cai, J. Wang, Z. Xu, Uncovering the design principle of conversion-based anode for potassium ion batteries *via* dimension engineering, Energy Stor. Mater. 34 (2021) 536–544, https://doi.org/10.1016/j.ensm.2020.10.017.
[24] W. Zhang, Y. Liu, Z. Guo, Approaching high-performance potassium-ion batteries *via* advanced design strategies and engineering, Sci. Adv. 5 (2019) eaav7412, https://doi.org/10.1126/sciadv.aav7412.
[25] R. Saroha, J.-H. Ahn, J.S. Cho, A short review on dissolved lithium polysulfide catholytes for advanced lithium-sulfur batteries, Korean J. Chem. Eng. 38 (2021) 461–474, https://doi.org/10.1007/s11814-020-0729-5.
[26] Z. Zhang, L. Duan, Y. Xu, C. Zhao, J. Bao, J. Shen, X. Zhou, Synthesis of multicore-shell FeS_2@C nanocapsules for stable potassium-ion batteries, J. Energy Chem. 73 (2022) 126–132, https://doi.org/10.1016/j.jechem.2022.04.039.
[27] Z. Wang, K. Dong, D. Wang, S. Luo, Y. Liu, Q. Wang, Y. Zhang, A. Hao, C. Shi, N. Zhao, Ultrafine SnO_2 nanoparticles encapsulated in 3D porous carbon as a high-performance anode material for potassium-ion batteries, J. Power Sources 441 (2019), 227191, https://doi.org/10.1016/j.jpowsour.2019.227191.
[28] A. Nulu, V. Nulu, K.Y. Sohn, Silicon and porous MWCNT composite as high capacity anode for lithium-ion batteries, Korean J. Chem. Eng. 37 (2020) 1795–1802, https://doi.org/10.1007/s11814-020-0559-5.
[29] Q.N. Tran, I.T. Kim, J. Hur, J.H. Kim, H.W. Choi, S.J. Park, Composite of nanocrystalline cellulose with tin dioxide as lightweight substrates for high-

performance lithium-ion battery, Korean J. Chem. Eng. 37 (2020) 898–904, https://doi.org/10.1007/s11814-020-0506-5.
[30] X. Zhao, W. Cai, Y. Yang, X. Song, Z. Neale, H.-E. Wang, J. Sui, G. Cao, $MoSe_2$ nanosheets perpendicularly grown on graphene with Mo–C bonding for sodium-ion capacitors, Nano Energy 47 (2018) 224–234, https://doi.org/10.1016/j.nanoen.2018.03.002.
[31] J.S. Lee, R. Saroha, J.S. Cho, Porous microspheres comprising $CoSe_2$ nanorods coated with N-doped graphitic C and polydopamine-derived C as anodes for long-lived Na-ion batteries, Nano-Micro lett. 14 (2022) 1–22, https://doi.org/10.1007/s40820-022-00855-z.
[32] F. Zheng, W. Zhong, Q. Deng, Q. Pan, X. Ou, Y. Liu, X. Xiong, C. Yang, Y. Chen, M. Liu, Three-dimensional (3D) flower-like $MoSe_2$/N-doped carbon composite as a long-life and high-rate anode material for sodium-ion batteries, Chem. Eng. J. 357 (2019) 226–236, https://doi.org/10.1016/j.cej.2018.09.105.
[33] Y. Liu, X. Yan, Y. Yu, X. Yang, Self-improving anodes for lithium-ion batteries: Continuous interlamellar spacing expansion induced capacity increase in polydopamine-derived nitrogen-doped carbon tubes during cycling, J. Mater. Chem. A 3 (2015) 20880–20885, https://doi.org/10.1039/c5ta05943g.
[34] L.L. Zhang, D. Ma, T. Li, J. Liu, X.K. Ding, Y.H. Huang, X.L. Yang, Polydopamine-derived nitrogen-doped carbon-covered $Na_3V_2(PO_4)_2F_3$ cathode material for high-performance Na-ion batteries, ACS Appl. Mater. Interfaces 10 (2018) 36851–36859, https://doi.org/10.1021/acsami.8b10299.
[35] A. Roy, A. Sarkar, M. Adil, S. Sau, N. Abharana, S. Mitra, Sodium-ion battery full-cell study with a pseudocapacitive $MoSe_2$-porous N-doped carbon composite anode and intercalated sodium vanadium fluorophosphate cathode, Batteries & Supercaps. 4 (2021) 978–988, https://doi.org/10.1002/batt.202100026.
[36] M.S. Jo, S. Ghosh, S.M. Jeong, Y.C. Kang, J.S. Cho, Coral-like yolk–shell-structured nickel oxide/carbon composite microspheres for high-performance Li-ion storage anodes, Nano-Micro lett. 11 (2019) 1–18, https://doi.org/10.1007/s40820-018-0234-0.
[37] Y.B. Dimitriev, S.I. Yordanov, L.I. Lakov, Formation and structure of glasses containing SeO_2, J. Non Cryst. Solids 192–193 (1995) 179–182, https://doi.org/10.1016/0022-3093(95)00348-7.
[38] W. Weisweiler, N. Subramanian, B. Terwiesch, Catalytic influence of metal melts on the graphitization of monolithic glasslike carbon, Carbon 9 (1971) 755-758, IN9-IN13, 759-761. https://doi.org/10.1016/0008-6223(71)90008-X.
[39] A. Oya, S. Ōtani, Catalytic graphitization of carbons by various metals, Carbon 17 (1979) 131–137, https://doi.org/10.1016/0008-6223(79)90020-4.
[40] Q. Yan, J. Li, X. Zhang, E.B. Hassan, C. Wang, J. Zhang, Z. Cai, Catalytic graphitization of kraft lignin to graphene-based structures with four different transitional metals, J. Nanoparticle Res. 20 (2018) 1, https://doi.org/10.1007/s11051-018-4317-0.
[41] Q. Liu, X. Li, Z. Xiao, Y. Zhou, H. Chen, A. Khalil, T. Xiang, J. Xu, W. Chu, X. Wu, Stable metallic 1T-WS_2 nanoribbons intercalated with ammonia ions: The correlation between structure and electrical/optical properties, Adv. Mater. 27 (2015) 4837–4844, https://doi.org/10.1002/adma.201502134.
[42] Y. Xia, B. Wang, X. Zhao, G. Wang, H. Wang, Core-shell composite of hierarchical MoS_2 nanosheets supported on graphitized hollow carbon microspheres for high performance lithium-ion batteries, Electrochim. Acta 187 (2016) 55–64, https://doi.org/10.1016/j.electacta.2015.11.047.
[43] J. Li, X. Lei, F. Qin, C. Zong, L. Liu, K. Zhang, $MoSe_2$ nanosheets embedded in mesoporous carbon as anode materials for sodium ion batteries, Ionics 25 (2019) 3143–3152, https://doi.org/10.1007/s11581-019-02889-7.
[44] D. Nam, J.U. Lee, H. Cheong, Excitation energy dependent raman spectrum of $MoSe_2$, Sci. Rep. 5 (2015) 17113, https://doi.org/10.1038/srep17113.
[45] L. Fang, Z. Lan, W. Guan, P. Zhou, N. Bahlawane, W. Sun, Y. Lu, C. Liang, M. Yan, Y. Jiang, Hetero-interface constructs ion reservoir to enhance conversion reaction kinetics for sodium/lithium storage, Energy Storage Mater. 18 (2019) 107–113, https://doi.org/10.1016/j.ensm.2018.10.002.
[46] G. Liu, H.H. Wu, Q. Meng, T. Zhang, D. Sun, X. Jin, D. Guo, N. Wu, X. Liu, J.-K. Kim, Role of the anatase/TiO_2 (B) heterointerface for ultrastable high-rate lithium and sodium energy storage performance, Nanoscale Horiz. 5 (2020) 150–162, https://doi.org/10.1039/C9NH00402E.
[47] M. Yousaf, Y. Wang, Y. Chen, Z. Wang, A. Firdous, Z. Ali, N. Mahmood, R. Zou, S. Guo, R.P.S. Han, A 3D trilayered CNT/$MoSe_2$/C heterostructure with an expanded $MoSe_2$ interlayer spacing for an efficient sodium storage, Adv. Energy Mater. 9 (2019) 1900567, https://doi.org/10.1002/aenm.201900567.
[48] Z. Luo, L. Zhou, L. Wang, G. Fang, A. Pan, S. Liang, Two-dimensional hybrid nanosheets of few layered $MoSe_2$ on reduced graphene oxide as anodes for long-cycle-life lithium-ion batteries, J. Mater. Chem. A 4 (2016) 15302–15308, https://doi.org/10.1039/C6TA04390A.
[49] D.J. Late, S.N. Shirodkar, U.V. Waghmare, V.P. Dravid, C.N.R. Rao, Thermal expansion, anharmonicity and temperature-dependent Raman spectra of single- and few-layer $MoSe_2$ and WSe_2, ChemPhysChem 15 (2014) 1592–1598, https://doi.org/10.1002/cphc.201400020.
[50] G. Jia, H. Wang, D. Chao, H. He, N.H. Tiep, Y. Zhang, Z. Zhang, H.J. Fan, Ultrathin $MoSe_2$@N-doped carbon composite nanospheres for stable Na-ion storage, Nanotechnology 28 (2017) 42LT01, https://doi.org/10.1088/1361-6528/aa8c55.
[51] S.Y. Jeong, S. Ghosh, J.-K. Kim, D.-W. Kang, S.M. Jeong, Y.C. Kang, J.S. Cho, Multi-channel-contained few-layered $MoSe_2$ nanosheet/N-doped carbon hybrid nanofibers prepared using diethylenetriamine as anodes for high-performance sodium-ion batteries, J. Ind. Eng. Chem. 75 (2019) 100–107, https://doi.org/10.1016/j.jiec.2019.03.007.
[52] J.H. Kim, Y.C. Kang, Synthesis of uniquely structured yolk-shell metal oxide microspheres filled with nitrogen-doped graphitic carbon with excellent Li-ion storage performance, Small 13 (2017) 1701585, https://doi.org/10.1002/smll.201701585.
[53] J. Ge, L. Fan, J. Wang, Q. Zhang, Z. Liu, E. Zhang, Q. Liu, X. Yu, B. Lu, $MoSe_2$/N-doped carbon as anodes for potassium-ion batteries, Adv. Energy Mater. 8 (2018) 1801477, https://doi.org/10.1002/aenm.201801477.
[54] Y. Yun, J. Shao, X. Shang, W. Wang, W. Huang, Q. Qu, H. Zheng, Simultaneously formed and embedding-type ternary $MoSe_2$/MoO_2/nitrogen-doped carbon for fast and stable Na-ion storage, Nanoscale Adv. 2 (2020) 1878–1885, https://doi.org/10.1039/c9na00815b.
[55] Q. Li, R. Cao, J. Cho, G. Wu, Nanocarbon electrocatalysts for oxygen reduction in alkaline media for advanced energy conversion and storage, Adv. Energy Mater. 4 (2014) 1301415, https://doi.org/10.1002/aenm.201301415.
[56] J.C. Groen, L.A. Peffer, J. Pérez-Ramírez, Pore size determination in modified micro-and mesoporous materials. Pitfalls and limitations in gas adsorption data analysis, Microporous Mesoporous Mater. 60 (2003) 1–17, https://doi.org/10.1016/S1387-1811(03)00339-1.
[57] P. Ge, L. Zhang, Y. Yang, W. Sun, Y. Hu, X. Ji, Advanced $MoSe_2$/carbon electrodes in Li/Na-ions batteries, Adv. Mater. Interfaces 7 (2020) 1901651, https://doi.org/10.1002/admi.201901651.
[58] L. Zeng, B. Kang, F. Luo, Y. Fang, C. Zheng, J. Liu, R. Liu, X. Li, Q. Chen, M. Wei, Facile synthesis of ultra-small few-layer nanostructured $MoSe_2$ embedded on N, P co-doped bio-carbon for high-performance half/full sodium-ion and potassium-ion batteries, Chem Eur J 25 (2019) 13411–13421, https://doi.org/10.1002/chem.201902899.
[59] Z.T. Shi, W. Kang, J. Xu, L.L. Sun, C. Wu, L. Wang, Y.Q. Yu, D.Y. Yu, W. Zhang, C. S. Lee, In situ carbon-doped $Mo(Se_{0.85}S_{0.15})_2$ hierarchical nanotubes as stable anodes for high-performance sodium-ion batteries, Small 11 (2015) 5667–5674, https://doi.org/10.1002/smll.201501360.
[60] Q. Su, X. Cao, T. Yu, X. Kong, Y. Wang, J. Chen, J. Lin, X. Xie, S. Liang, A. Pan, Binding $MoSe_2$ with dual protection carbon for high-performance sodium storage, J. Mater. Chem. A 7 (2019) 22871–22878, https://doi.org/10.1039/C9TA06870H.
[61] H. Kim, K. Lim, G. Yoon, J.H. Park, K. Ku, H.D. Lim, Y.E. Sung, K. Kang, Exploiting lithium–ether Co-intercalation in graphite for high-power lithium-ion batteries, Adv. Energy Mater. 7 (2017) 1700418, https://doi.org/10.1002/aenm.201700418.
[62] L.-B. Tang, B. Zhang, C.-S. An, H. Li, B. Xiao, J.-H. Li, Z.-J. He, J.-C. Zheng, Ultrahigh-rate behavior anode materials of $MoSe_2$ nanosheets anchored on dual-heteroatoms functionalized graphene for sodium-ion batteries, Inorg. Chem. 58 (2019) 8169–8178, https://doi.org/10.1021/acs.inorgchem.9b00971.
[63] L. Zeng, Y. Fang, L. Xu, C. Zheng, M.-Q. Yang, J. He, H. Xue, Q. Qian, M. Wei, Q. Chen, Rational design of few-layer $MoSe_2$ confined within ZnSe–C hollow porous spheres for high-performance lithium-ion and sodium-ion batteries, Nanoscale 11 (2019) 6766–6775, https://doi.org/10.1039/C9NR00146H.
[64] F. Luo, X. Feng, L. Zeng, L. Lin, X. Li, B. Kang, L. Xiao, Q. Chen, M. Wei, Q. Qian, In situ simultaneous encapsulation of defective MoS_2 nanolayers and sulfur nanodots into SPAN fibers for high rate sodium-ion batteries, Chem. Eng. J. 404 (2021), 126430, https://doi.org/10.1016/j.cej.2020.126430.
[65] S.H. Oh, S.M. Park, D.-W. Kang, Y.C. Kang, J.S. Cho, Fibrous network of highly integrated carbon nanotubes/MoO_3 composite bundles anchored with MoO_3 nanoplates for superior lithium ion battery anodes, J. Ind. Eng. Chem. 83 (2020) 438–448, https://doi.org/10.1016/j.jiec.2019.12.017.
[66] J.-S. Park, J.S. Cho, J.H. Kim, Y.J. Choi, Y.C. Kang, Electrochemical properties of micron-sized Co_3O_4 hollow powders consisting of size controlled hollow nanospheres, J. Alloy. Compd. 689 (2016) 554–563, https://doi.org/10.1016/j.jallcom.2016.07.233.
[67] B.-I. Park, J.-S. Park, S. Yu, S.-H. Cho, J.Y. Byun, J. Oh, S.Y. Lee, Hollow/porous-walled SnO_2 *via* nanoscale kirkendall diffusion with irregular particles, Acta Mater. 186 (2020) 20–28, https://doi.org/10.1016/j.actamat.2019.12.039.
[68] Q. Jiang, L. Wang, Y. Wang, M. Qin, R. Wu, Z. Huang, H.-J. Yang, Y. Li, T. Zhou, J. Hu, Rational design of $MoSe_2$ nanosheet-coated MOF-derived N-doped porous carbon polyhedron for potassium storage, J. Colloid Interface Sci. 600 (2021) 430–439, https://doi.org/10.1016/j.jcis.2021.05.050.
[69] W. Liu, J. Yuan, Y. Hao, H.M.K. Sari, J. Wang, A. Kakimov, W. Xiao, J. Qin, W. Li, C. Xie, Heterogeneous structured $MoSe_2$–MoO_3 quantum dots with enhanced sodium/potassium storage, J. Mater. Chem. A 8 (2020) 23395–23403, https://doi.org/10.1039/D0TA08674F.
[70] L. Yu, G. Wang, J. Gao, J. Li, B. Peng, G. Zhang, Sacrificial nanowire catalyzed polymerization process generates hierarchical $MoSe_2$ grafted carbonaceous nanotubes for superior potassium ion storage, ACS Appl. Energy Mater. 4 (2021) 6757–6767, https://doi.org/10.1021/acsaem.1c00864.